One century of tectonic deformation along the Sumatran Fault from triangulation and GPS surveys

L. Prawirodirdjo, Y. Bock, J. F. Genrich

Cecil H. and Ida M. Green Institute of Geophysics and Planetary Physics, Scripps Institution of Oceanography, University of California, San Diego, 9500 Gilman Drive, La Jolla, California 92093-0225 *(phone: (858)822-0557; fax: (858) 534-9873; email:* linette@josh.ucsd.edu, ybock@ucsd.edu, jeff@josh.ucsd.edu)

S. S. O. Puntodewo, J. Rais, C. Subarya, S. Sutisna

National Coordination Agency for Surveying and Mapping, Jl. Raya Jakarta Bogor km 46, Cibinong, Indonesia (*email:* geodesi@server.indo.net)

Abstract. An analysis combining historical triangulation and recent Global Positioning System (GPS) survey measurements in West and North Sumatra, Indonesia, reveals a detailed slip history along the central part of the Sumatran Fault. The arc-parallel components of the combined velocity field are consistent with slip rates inferred from GPS data, ranging from 23 to 24 mm/yr. Between 1.0°S and 1.3°N the Sumatran Fault appears to be characterized by deep locking depths, on the order of 20 km, and the occurrence of large (M_w ~ 7) earthquakes. The long-term (1883-1993) strains show simple right-lateral shear, with rates similar to GPS-measured, 1989-1993 strain rates. Coseismic deformation due to the 1892 Tapanuli and 1926 Padang Panjang earthquakes, estimated from triangulation measurements taken before and after the events, indicate that the main shocks were significantly larger than previously reported. The 1892 earthquake had a likely magnitude of $M_w \approx 7.6$, while the 1926 events appear to be comparable in size to the subsequent (M ~ 7) 1943 events, and an order of magnitude higher than previously reported.

Introduction

The first geodetic measurements of coseismic deformation were made by serendipity on the island of Sumatra during the course of a triangulation survey [*Müller*, 1895]. These data, which indicated right-lateral motion in a NW-SE direction, were later referenced by *Reid* [1913] as evidence for his elastic rebound theory of the earthquake cycle. The triangulation survey was part of an extensive geodetic network established by the Dutch colonial government in the 1880s and 1890s. The entire triangulation network consisted of more than 2000 primary, secondary, and tertiary sites, covering most of the island [*Triangulatiebrigade van den Topographischen Dienst*, 1916; *War Research Institute*, 1944]. Construction of a concrete pillar and subsequent initial surveys often took several weeks at each site. Because triangulation involved point-to-point optical direction readings through a theodolite, most stations were situated on mountain tops. The Sumatran Fault (SF) extends over the entire length of the island (~1600 km) through the Bukit Barisan mountains and the volcanic chain (Figure 1), and was thus conveniently well-spanned by the triangulation network.

We initiated GPS geodetic surveys in Sumatra in 1989 [*Bock et al.*, 1990; *McCaffrey et al.*, 1990] as part of a larger campaign which included the entire Indonesian archipelago [*Puntodewo et al.*, 1994; *Genrich et al.*, 1996; *Prawirodirdjo et al.*, 1997, *Stevens et al.*, 1999]. In this paper, we describe crustal deformation in the vicinity of the SF inferred from triangulation and GPS data spanning a period of over 100 years. The triangulation data were available to us from historical archives and provided the intriguing opportunity to test whether recent GPS-measured deformation rates are consistent with longer-term rates, if we could re-occupy some of the triangulation pillars with GPS. Many of the triangulation monuments are in remote areas that even with modern logistics represent a formidable challenge for state-of-the-art, space-based geodetic surveys. Furthermore, as we discovered during the reconnaissance phase of the project, the state of preservation of the triangulation pillars usually correlated inversely with accessibility.

The GPS network on Sumatra came to include 22 historical triangulation sites, and was surveyed from 1989 to 1993, (see also *Genrich et al.*, [this volume]). The subset

of triangulation sites we call the "West Sumatra" network (Figure 2, Table 1), established between 1883 and 1896 at 1.5°S to 2°N latitude, is especially useful for comparing crustal deformation rates because many of its sites were surveyed at more than one epoch with triangulation, and were also surveyed during the 1989-1993 GPS campaigns. In addition, we used several sites from the "North Sumatra" network (north of 2°N, Figure 2, Table 1), established between 1907 and 1918, which were reoccupied with GPS.

Several studies [e.g., *Snay and Drew*, 1989; *Grant*, 1990] have shown it feasible to combine space geodetic and terrestrial survey data to derive an unambiguous velocity field. *Dong* [1993] and *Dong et al.* [1998] subsequently developed a theoretically rigorous method for combining heterogeneous geodetic data sets based on the work of *Hein* [1986] and *Collier et al.* [1988]. This method, which we applied here, was implemented in the software package FONDA, developed by *Dong* [1993].

The ability to combine heterogeneous data sets with widely differing measurement epochs and scenarios is important for two reasons. First, it allows us to extend the relatively short temporal coverage of space geodetic data by combining them with terrestrial geodetic data which in Sumatra date as early as the late 19th century. Furthermore, the addition of space geodetic data lets us eliminate the rank deficiencies inherent in terrestrial geodetic data without applying arbitrary external constraints, such as, for example, the "inner coordinate" constraint [*Segall and Matthews*, 1988].

We performed a network adjustment of the combined triangulation and GPS data to obtain an averaged deformation field over the last 100 years, which we then compare to the short term (4-year) GPS-derived deformation. We examined whether our combined velocity field is consistent with slip rates and locking depths inferred from GPS measurements and geological observations. In addition, we estimated the coseismic deformation caused by the 1892 [*Reid*, 1913], 1926 ($M_s \approx 6.5$ and 6.8, [*Gutenberg and Richter*, 1954]) and 1943 ($M_s \approx 7.1$ and 7.4, [*Pacheco and Sykes*, 1992]) earthquakes. We discuss our results in the context of a recent, comprehensive geological study of the SF by *Sieh and Natawidjaja* [this volume], as well as comparing them to results from the GPS surveys reported by *Genrich et al.* [this volume] with further analysis by *McCaffrey et al.* [this volume].

Sumatra Tectonics

Sumatra experiences active deformation and large earthquakes due to subduction of the Australian plate beneath Southeast Asia [e.g., *Newcomb and McCann*, 1987]. From velocity vectors derived from regional GPS data [*Prawirodirdjo*, 2000], the pole of rotation for the Australian plate relative to Southeast Asia is located in East Africa (9.64 ± 1.44°N, 51.38 ± 2.03°E), with an angular rotation rate of 0.677 ± 0.016°/Myr. Thus, southwest of Sumatra, the convergence of the Australia plate occurs obliquely, ranging from 60 mm/yr, N17°E azimuth at (6°S, 102°E) to 52 mm/yr, N10°E azimuth at (2°N, 95°E) (Figure 1). The oblique convergence is partitioned into subduction at the trench which is nearly perpendicular to the arc, and arc-parallel motion of the forearc along the SF [*Fitch*, 1972; *McCaffrey*, 1991]. *McCaffrey* [1991] further demonstrated from earthquake slip vector deflections and plate convergence vectors that the forearc sliver plate located between the trench and the SF is not rigid, but instead undergoes arc-parallel stretching, requiring a northwestward increase in slip rate along the SF. Slip rates estimated at two locations by *Sieh et al.* [1991] from stream offsets incised in Quaternary volcanic tuffs, and at several locations by *Bellier and Sébrier* [1995] from SPOT satellite images of stream offsets, support an increase in slip rates from SE to NW. However, recent GPS surveys [*Genrich et al.* this volume] show only a marginal increase.

The spatial and temporal variations in slip rate and seismicity along the SF are still only poorly known. The spatial variations are just beginning to be revealed by geodetic and geologic observations. While it is confirmed that the oblique convergence is generally partitioned into subduction at the trench and transcurrent shear along the SF, modeling of geodetic data shows that this simple scenario is complicated by many intriguing details. There appears to be a North-South segmentation in the pattern of strain accumulation along the subduction zone [*Prawirodirdjo et al.*, 1997]. The southern half of the forearc is moving roughly in the same direction as the convergence between the Australia plate and Southeast Asia, while the northern half is moving in a direction more closely parallel to the arc. The division of the forearc velocity field coincides with the boundary between the rupture zones of the 1833 and 1861 ($M_W > 8$) thrust earthquakes

postulated by *Newcomb and McCann* [1987], and is thus probably related to the subduction zone's rupture kinematics. Also, the inferred slip rate on the SF is about 1/3 less than the full arc-parallel component of plate motion [*McCaffrey et al.*, this volume]. To account for 20 km of offset on the SF since the Oligocene [*Sieh and Natawidjaja*, this volume], an additional 20 mm/yr of strike-slip is required west of the SF, and probably takes place seaward of the Mentawai islands [*McCaffrey et al.*, this volume].

Our goal in this study, together with those presented by *Genrich et al.* [this volume] and *McCaffrey et al.* [this volume], is to gain some insight into the spatial and temporal details of the dynamics along the SF. Moreover, since rupture kinematics along the SF and in the forearc are strongly correlated with structural features, it is important that we formulate interpretations of our geodetic data consistent with geological observations such as those made by *Sieh and Natawidjaja* [this volume]. Throughout this paper, in referring to various regions along the SF, we use the fault segment names proposed by *Sieh and Natawidjaja* [this volume].

Data

Triangulation data

The original triangulation monuments consisted of concrete pillars about 1.5 m high, with embedded bronze markers (Figure 3). Horizontal angles from a central station to a set of surrounding stations were measured using micro-theodolites, from Pistor & Martins and Wegener & Wanschaff, and heliotropes placed on the pillars with their axes in the plumb-line of the bronze markers [*War Research Institute*, 1944].

We used 391 horizontal angle measurements from the West and North Sumatra networks, defining 106, roughly equilateral triangles (Figure 2), with sides measuring 20 to 70 km long. For each network there were also available one distance measurement and one azimuth measurement, intended to fix the scale and orientation of the network. The distance measurements were not precise enough, however, to constrain the scale to within less than several hundred parts per million (ppm). Nor are the azimuth measurements useful to us, since they were taken at sites where we do not know the coordinates precisely. Instead, we fixed scale and orientation by linking GPS and triangulation

horizontal positions and velocities at well-determined, collocated stations, as described in a later section of this paper.

The initial survey of the West Sumatra network began in 1883 and was completed in 1896. The North Sumatra network was surveyed in 1907-1916. After the 1926 Padang Panjang earthquake (Figure 2), sites around the rupture area were resurveyed in 1927-1930. At the Angkola segment of the SF (1°N latitude, Figure 2), an earthquake occurred in 1892 while a second-order survey was underway, displacing the triangulation monuments [*Müller*, 1895; *Reid*, 1913]. Sites near the rupture area were later surveyed again over the next two years (1892-1894). For reasons unknown to us, repeat measurements were also performed in 1917 and 1918 at a few sites in the West Sumatra network (Figure 2), and in 1930 in the North Sumatra network (Figure 2). Table 1 summarizes the triangulation sites and their dates of survey.

The original raw data were reduced by one of us (*Sutisna*) to one measurement for each angle and then used as input to a least-squares adjustment of station coordinates using the software package CHAOS (School of Surveying, University of New South Wales). The ancillary distance and azimuth measurements mentioned above were used to nominally constrain the scale and orientation of the network. The result of this adjustment was a set of station coordinates referenced to the GRS67 ellipsoid. We used these as a priori triangulation site coordinates. The GRS67 is based on the geocentric equipotential ellipsoid, with ellipsoid parameters (ellipticity f = 1/298.2472 and semi-axis length a = 6,378,160.00 m [*International Association of Geodesy*, 1971]) significantly different from the WGS84 ellipsoid (f = 1/298.257223563, a = 6,378,137.00 m [*Defense Mapping Agency*, 1987]), to which our GPS geodetic coordinates are referenced. Hence, before combining the data, we transformed the triangulation coordinates into the WGS84 system by converting them into geocentric Cartesian coordinates and converting them back to geodetic coordinates using the WGS84 ellipsoid parameters.

GPS Data

Our analysis is based on GPS data from geodetic surveys performed in Sumatra in 1989, 1990, 1991, and 1993. Some sites in South and East Sumatra were surveyed in

1994 but these measurements are not used in this analysis. Neither did we use data from the near-field arrays, discussed by *Genrich et al.* [this volume], which were part of the Sumatra GPS surveys. A detailed description of the GPS campaigns in Sumatra can be found in *Prawirodirdjo* [2000], and the complete GPS velocity field is documented in *Genrich et al.* [this volume].

Dual-frequency carrier phase and pseudorange observations were combined with improved orbits [*Fang and Bock*, 1996] to compute daily solutions consisting of site coordinates, satellite state vectors, tropospheric zenith delay parameters, and phase ambiguities by weighted least squares using GAMIT version 9.40 [*King and Bock*, 1995]. The daily solutions were then combined using GLOBK version 4.12 and GLORG version 4.04 [*Herring*, 1997] to estimate site coordinates and velocities. North and east velocity components have a typical formal one standard deviation (assuming a white noise stochastic model for the estimated site coordinates - see *Zhang et al.* [1997]) of 1-2 mm/yr and 3-4 mm/yr, respectively.

Of more than 70 GPS sites surveyed, 22 were located on triangulation sites. A 4-day GPS survey of a well-preserved site typically required a one day vehicle drive to the nearest village, assembly of a team of local guides and porters, a 1-3 day ascent to the site on previously non-existing or barely established narrow mountain trails, several hours of site perimeter clearing to gain reasonable satellite visibility, the actual 4-day GPS survey, and a 1-2 day return trip to the village.

The triangulation sites that were reoccupied during the GPS campaigns fall roughly into three categories:

- Sites whose monuments were sufficiently intact so that they were resurveyed directly over the original bronze marker (Figures 3A-C). At least four sites, P106/DOLO, P109/DSIM, S059/MERA, and S200/SIGL (Figure 2, Table 2), fall within this category. We refer to these as the "core" sites.
- Sites whose monuments were still erect but had sustained some damage, including removal of the bronze marker. At these sites, the GPS antenna was set up over the remains of the monument (Figure 3D), approximating the location of the triangulation marker to within a few tens of centimeters.

- Sites whose monument had sustained heavy damage or had been completely destroyed, requiring construction of a new monument over the likely location of the original mark. GPS re-occupation was performed within one meter of the estimated original mark (Figure 3E).

In addition, in an attempt to tie in eight more triangulation sites, we established new monuments placed as close to the original sites as local logistics permitted (up to several km). Although GPS vectors were measured from these eight eccentric sites to the respective triangulation sites, the measurements were, unfortunately, not precise enough to serve as ties in our analysis. We used one of these eccentric sites (DEMU) to establish a reference frame in the northern part of the network, by linking its horizontal velocity to that of its corresponding triangulation monument (P065). Table 2 summarizes the relationships between the triangulation and GPS stations.

The triangulation stations which were resurveyed with GPS were used to update the a priori triangulation site coordinates. Using FONDA, we used the GPS-measured velocities of the collocated stations to propagate back in time to estimate coordinates of the collocated stations during the triangulation epochs, and used the angle measurements to estimate coordinates for all other triangulation stations not resurveyed with GPS. This process, described in more detail in a later subsection of this paper, yielded improved coordinates for all the triangulation stations, and allowed us to assume, in subsequent analyses, that the coordinates for most of the triangulation stations are well determined. In this manner, information from the GPS measurements allowed us to eliminate the rank deficiencies of the triangulation data.

Analysis

Our analysis of the triangulation and GPS measurements was based on the method developed by *Dong* [1993] and *Dong et al.* [1998], to analyze trilateration and GPS data in southern California. This method is implemented in the software package FONDA [*Dong,* 1993], a sequential least-squares (Kalman filter) estimation in which station positions are estimated as a function of time, taking into account secular velocities

and, where appropriate, episodic and stochastic station displacements. The method is briefly reviewed here.

First, loosely constrained estimates of geodetic parameters are obtained from an analysis of individual experiments to serve as "quasi-observations" for the combined solution. Here we derived loosely constrained estimates of site positions from the 1989-1993 GPS observations, and the angle measurements from triangulation surveys. The "quasi observations" are then combined using FONDA. Unknown episodic (coseismic) site displacements at a subset of specified sites are modeled as step functions in the site positions. General constraints on position and site velocity were imposed on the solution to remove the rank deficiency in the triangulation data, and to define a uniform reference frame through well-determined stations common to all data sets. Including data from a global network in the analysis of primary GPS observations renders the GPS solution unambiguous on the regional scale. Thus, by linking GPS and triangulation estimates of horizontal velocities of well-determined, collocated stations, we removed the dilatation and rotation ambiguity inherent in the triangulation surveys [*Dong et al.*, 1998].

FONDA's estimation procedure yields site coordinates, velocities, and episodic (in this case, coseismic) displacements simultaneously. However, we chose not to estimate all the desired parameters in one large solution involving all the triangulation and GPS data. We opted instead for a slightly distributed approach, with the goal of minimizing the effect of any systematic shifts on the displacement and velocity estimates. For example, to estimate coseismic displacements spanned by triangulation surveys, we used only subsets of angle measurements from before and after the earthquake (and site coordinates updated using the GPS measurements). To estimate long-term interseismic strain, we used the first-epoch triangulation measurements and GPS data, accounting for coseismic displacements by applying corrections based on the coseismic estimation. More detailed descriptions of the procedures used at each step are given in the following subsections.

Assessment of triangulation data quality

To estimate the error in the triangulation (angle) measurements, we inverted the triangulation data set for station coordinates only. Holding fixed the coordinates of two arbitrarily chosen sites, P037 and P042 (Figure 2), eliminates the rank deficiency due to scale and orientation. In this inversion we did not include measurements taken by *Müller* [1895] in the epicentral area immediately after the 1892 earthquake, since we expected them to contain large contributions from the earthquake. Figure 4 shows the distribution of angle residuals from this adjustment of 374 angle measurements from 82 sites. We found that repeating this adjustment while holding coordinates of different pairs of sites fixed did not significantly affect the distribution of residuals. With the exception of angles measured from station P009, the RMS residuals of angles measured from each station all fall below 0.5 arc seconds. The standard deviation of the residuals is 0.4 arc seconds. This corresponds to about 2 ppm in triangle misclosure [*Davies et al.*, 1997], the difference between the sum of three angles in a given triangle and 180° plus the spherical excess [*Bomford*, 1980; *Yu and Segall*, 1996]. This level of precision is adequate to detect regional strains, which are expected to be a few tens of ppm over 100 years (the interval between triangulation and GPS surveys) or several ppm over about 45 years (the interval between repeated triangulation measurements in the region of the 1926 and 1943 earthquakes, Figure 2).

Updating site coordinates

First, we estimated four transformation parameters (3D translation and rotation about one axis) based on the collocated sites indicated in Table 2. A coordinate transformation was then performed to align the a priori triangulation site coordinates with the GPS coordinate system. This first step serves as a large-scale correction to the a priori triangulation site coordinates, while still disregarding the temporal variations in site positions.

Next, we used FONDA to adjust the triangulation site coordinates, using all the angle measurements. In this adjustment, the positions and velocities of the four core sites

(P106, P109, S059 and S200) are tightly constrained to their GPS-determined values. In addition, velocities (but not the positions) of triangulation sites where the GPS resurveys were within tens of centimeters of the original mark, were constrained to their GPS-determined values. Beginning with strict outlier identification criteria, we repeated the adjustment a few times, updating coordinates and loosening the outlier identification criteria after each iteration. In the final adjustment, we constrained the horizontal coordinates of the GPS-resurveyed triangulation sites to within 20 cm, and of the four core sites to within 1 cm of their GPS-determined positions (the coordinate constraints were loosened up again when we began estimating deformation rates). By thus using the GPS-measured velocities of the collocated stations, FONDA propagates back in time to estimate coordinates of the collocated stations during the triangulation epochs, and uses the angle measurements to estimate coordinates for all other triangulation stations not resurveyed with GPS. This process yielded improved coordinates for all the triangulation sites to be used in the velocity field estimation.

Our final adjustment included 357 angle measurements for 87 stations. All angle measurements were given equal weight. We did not estimate vertical velocities, and vertical positions (heights) were given tight constraints. After the final iteration, the postfit RMS of the angle measurements was 0.9 arc seconds. This level of error, higher than the 0.4-0.5 arc seconds obtained from our initial adjustment of angle measurements, suggests that some stations may have experience coseismic as well secular motion. Nevertheless, these updated coordinates are sufficient in quality to be used as a priori values in the studies that follow. Three measurements, all taken from site S080, were discarded due to large angle residuals.

Results and Discussion

Interseismic deformation rates obtained by combining triangulation and GPS measurements

By performing a solution combining first-epoch triangulation measurements for the West and North Sumatra networks with GPS measurements, we estimated the long-term interseismic deformation rates. ITRF96 [*Sillard et al.*, 1998] -based locations served

as a priori coordinates for the GPS sites, and the set of updated coordinates described above as those for the triangulation sites. Since the interval between the triangulation and GPS surveys also spans the 1943 earthquake, we solved for coseismic displacements at sites near the 1943 rupture zone along with the interseismic deformation rates (see later subsection on the 1943 earthquakes).

As quasi-observations for the GPS-reoccupied sites (listed in Table 2), we used loosely constrained coordinates obtained from analysis of the entire GPS data set. For sites surveyed both by triangulation and GPS, our goal was to obtain the long-term (1880s–1990s) velocities from the a priori triangulation coordinates, angle measurements, and current GPS positions. To minimize dependence on the short-term (GPS-measured) velocity signal, we did not want to include GPS-measured velocities as quasi-observations (although note that the GPS velocities have been used to update the triangulation site coordinates). However, we included the GPS-measured velocity for one site, DEMU, as a quasi-observation in our adjustment. This site is eccentric to P065, and we constrained P065 to have the same velocity as DEMU to install a frame of reference for velocities in the northern part of the triangulation network. Both sites, only 8 km apart, are located in the back-arc basin, where strain rates are very small (~0.01 μstrain/yr, [*McCaffrey et al.*, this volume], Table 3). As input from the triangulation surveys, we used all available first-epoch angle measurements for the West and North Sumatra networks. This included several sites which were surveyed only once, which are needed for triangle closure (we did not estimate their velocities).

Following *Dong's* [1993] approach, we first combined the triangulation and GPS observations in a loosely-constrained solution. We then applied constraints to P042 and P065. We constrained the position and horizontal velocity of P042, which is located on the back-arc, to their GPS-derived, ITRF96 values. As mentioned above, we also constrained P065 to have the same velocity as DEMU, but did not constrain its position. The constraints on P042 and P065 placed the estimated velocity field in the ITRF96 reference frame and allowed us to make a direct comparison between the long-term velocities derived here and the GPS-measured velocities. In this process, the only assumptions we made are that two sites (DEMU and P042/PAUH) located on the back-

arc have had a constant velocity (as measured by GPS) during the period between the triangulation and GPS surveys, and that P065 moves at the same (constant) velocity as DEMU.

The velocity field for 1883-1993 obtained from the combined solution of triangulation and GPS measurements is shown in Figure 5, plotted relative to the Eurasia plate pole of rotation. This does not include the measurements made in 1927-1930. For comparison, the short-term GPS-derived velocities have also been included.

At sites P005, P015, P017, P106, and P109, long-term and short-term rates agree within their 95% confidence regions (Figure 5). The long-term velocities south of the equator clearly show right-lateral shear across the SF. Sites located around the Suliti and Siulak segments (south of 1.5°S), are only weakly connected to the rest of the West Sumatra network, yet the velocity field in this area clearly shows right-lateral shear across the SF. The velocities in the northern back-arc (north of 1.5°N) have large uncertainties, but the uniformity of the vectors suggests lack of internal deformation in that region of the back-arc.

Genrich et al. [this volume] inferred slip rates and locking depths along the SF by fitting GPS-measured velocities to *Savage and Burford's* [1973] 1-D elastic dislocation model for a locked strike-slip fault. In this model, velocities located far (> 100 km) from the fault trace largely constrain the slip rate, while velocities near the fault constrain the locking depth. Vectors from the combined triangulation and GPS solution all lie within 150 km of the SF, are sparsely distributed, and have large uncertainties, hence they only loosely constrain slip rate and locking depth. Therefore, we did not attempt to infer slip rates or locking depths from our combined velocities, but in Figure 6 we compare them to the slip rates and locking depths estimated by *Genrich et al.* [this volume]. Because convergence between the Australia plate and the forearc is nearly perpendicular to the trench, strain accumulation on the subduction zone mainly affects the arc-normal components of the vectors, while the arc-parallel components reflect slip along the SF [*Prawirodirdjo et al.*, 1997]. Hence we plotted (Figure 6) the arc-parallel velocities for four regions across the SF corresponding to segments reported by *Sieh and Natawidjaja*

[this volume], with curves reflecting slip rates and locking depths estimated by *Genrich et al.* [this volume] from GPS data at the appropriate latitudes.

Our combined velocities at the Toru segment (approximately 2° to 3.5°N) are consistent with a slip rate of 24 mm/yr and a locking depth of 9 km reported by *Genrich et al.* [this volume] for this region (Figure 6A).

Between 0° and 1.8°N, the SF splits into two major strands (the Barumun and Angkola segments, Figure 1), and thus cannot be modeled by a simple fit to *Savage and Burford's* [1973] model. Assuming locking depths of 10-20 km and treating the vectors as the sum of surface deformation due to slip on both fault branches, *Genrich et al.* [this volume] estimated slip rates of 2-4 mm/yr on the eastern (Barumun) branch and 19-21 mm/yr on the western (Angkola) branch. In this region, all our combined vectors have large uncertainties. Within the 95% confidence level, the arc-parallel components of our vectors at P040 and S059 are consistent with either the GPS-measured values or with zero slip (Figure 6B). The large discrepancy at P051 may indicate that we underestimated the error in locating the former triangulation site.

Along the Sianok and Sumani segments (approximately 1.0° to 0.5°S), our velocity vectors are also scattered and include a few anomalously high velocities, noticeably at P001, P002, P004 and P027. Our results suggest slip rates closer to *Genrich et al.'s* [this volume] estimate of 23 mm/yr (Figures 6C and 6D) than *Natawidjaja and Sieh's* [1994] estimate of 12 mm/yr at these latitudes. Our data at Sumani and Sianok appear to favor locking depths on the order of 20 km.

South of 1°S, along the Suliti and Siulak segments, velocity estimates are available only from the triangulation data. In Figure 6E we plot the fault-parallel velocities in this region, along with a curve showing the same slip rate and locking depth as the Sumani segment (just north of Suliti). Although the uncertainties are large, our velocity field for the Suliti-Siulak segments is similar to our combined velocity field for the Sumani segment, suggesting a slip rate also closer to ~20 mm/yr or higher instead of ~10 mm/yr as reported by *Sieh et al.* [1991] and *Natawidjaja and Sieh* [1994] for this region.

Deep locking depths inferred by *Genrich et al.* [this volume] in the Sumani, Sianok, and Angkola regions are consistent with the occurrence of $M_s \geq 7$ earthquakes in 1822, 1892, 1926 and 1943 [*Müller*, 1895; *Visser* 1927; *Untung et al.*, 1985; *Natawidjaja et al.*, 1995]. Analysis of the triangulation data, in combination with GPS measurements, support the results suggested by Genrich et al. [this volume] that, on time scales of ~100 years, the SF can be characterized by deep locking depths which result in large ($M_w \geq 7$) earthquakes.

Strain rates

As mentioned before, parts of the triangulation network have more than one epoch of angle measurements. These include sites around the Sianok and Sumani segments which were surveyed in 1883-1885 and again in 1927-1930, and sites in the northern back-arc, just SE of Lake Toba, which were surveyed in the 1890s and again in 1930. For these intervals we could not determine an unambiguous velocity field, but we estimated strain rates which we then compared to strain rates computed from GPS measurements.

Five sites around the Suliti and Siulak segments (P024, P026, P030, P033, and P034; Figure 2) also have two epochs of angle measurements, from 1887-1890 and 1917-1918. Also in this region and connected to those stations, P038 and P039 were surveyed twice, once in 1888-1890 and again in 1904. However, data from this region along the Suliti and Siulak segments were not enough to yield a meaningful strain solution.

Sumani region

For the region around the Sumani segment, we estimated strain rates for the period 1883-1930 from two epochs of triangulation data, and for the period 1883-1993 from triangulation and GPS data.

Strain rates from the two epochs of triangulation data (1883-1885 and 1927-1930) were computed from the angle measurements using the program ADJCOORD [*Bibby*, 1982; *Crook*, 1992], and are expressed in terms of the "engineering" shear strain rates, $\dot{\gamma}_1$ and $\dot{\gamma}_2$ [*Feigl et al.*, 1990] (Table 3). Scale and orientation were fixed by

constraining the horizontal coordinates of P001, and the azimuth and distance from P001 to P007. These triangulation measurements across the Sumani segment for 1883-1930 span the 1926 earthquakes. However, effects of the earthquakes are not evident in the shear strains listed in Table 3. The values of $\dot{\gamma}_1$ and $\dot{\gamma}_2$ are consistent with strain rates estimated by *McCaffrey et al.* [this volume] from GPS measurements (Table 3).

Strain rates from 1883 to 1993 spanned by the triangulation and GPS data were computed by fitting a surface strain rate tensor to the velocity field (described in the previous subsection), then finding the magnitudes and directions of the principal strain rate components [*Feigl et al.*, 1990]. The strain rates are given in Table 3. We note, however, that the tensor components are not uniquely determined by the triangulation measurements, and are dependent on our assumptions about the GPS data. Therefore, we interpret only the engineering strains, $\dot{\gamma}_1$ and $\dot{\gamma}_2$. Strain rates across the Sumani segment computed from 1883-1885 triangulation and 1989-1993 GPS data are consistent with right-lateral shear strain parallel to the SF. Furthermore, the shear strain rates $\dot{\gamma}_1$ and $\dot{\gamma}_2$ are consistent, within the uncertainties, with those estimated by *McCaffrey et al.* [this volume] from GPS measurements (Table 3). Since measurements from 1927-1930 were not included in the estimation, strain rates for this period (1883-1993) are probably even less sensitive to effects of the 1926 earthquake than the 1883-1927 strain rates, and are likely to reflect the long-term interseismic strains. Since the GPS-measured strain rates are consistent with these strain rates, we infer that the GPS-measured strain rates are a good indication of the long-term, interseismic deformation.

Northern back-arc

We estimated strain rates from the two epochs (1894-1895 and 1930) of angle measurements taken in the northern back-arc region (stations P055, P058, P060, P062, P063, and P064; Figure 2) using ADJCOORD, constraining the horizontal position of P062 and the azimuth and distance from P062 to P064. The error estimates are much larger than the strain rate estimates (Table 3), so we cannot draw any firm conclusions. However, the results suggest that the strain rates are probably much smaller than strain rates at the Sumani segment. A similar level of strain (~0.01 μstrain/yr) is estimated by

McCaffrey et al. [2000] for the central back-arc (Table 3), suggesting that the back-arc region east of the SF is relatively free of deformation. This result was also reflected in the velocity field for the northern back-arc region (Figure 5).

Estimation of coseismic deformation

1892 earthquake

For the 1892 earthquake, a direct estimate of the coseismic deformation from monument displacements is available from surveyors at the scene [*Müller*, 1895; *Reid*, 1913], but there exists no reliable estimate of the event's magnitude. One of our goals in analyzing these data was to estimate the size of the 1892 earthquake. Triangulation surveys in the region of the Angkola segment (Figure 1) were started by *Müller* in 1890. After the 1892 Tapanuli earthquake, sites surrounding the epicentral region were resurveyed from 1892 through 1895. *Müller's* measurements in this area were later connected to the rest of the Sumatra networks by only one measurement, and thus form a semi-independent data set (they were published as such in *Müller* [1895]). To estimate the 1892 coseismic displacements, we performed an adjustment of *Müller's* 1890-1895 Tapanuli measurements for seven sites in the region (Figure 7A), solving for surface coseismic displacements. We used coordinates for these sites which have been updated using GPS measurements (see previous subsection). Making the assumption that the GPS-measured velocities are representative of the long-term, we fix scale and orientation by constraining the coordinates of five stations (all but S063 and S080) to their updated values. Stations S063 and S080 were not included in the preliminary network adjustment performed by *Sutisna* and were not surveyed with GPS (attempts to locate these two sites were unsuccessful), so we do not have good a priori coordinates for them. Hence, coordinates for S063 and S080 were given looser constraints (0.5 meters) in the adjustment.

Since all measurements included in the adjustment were taken within a time span of three years (and most measurements were taken within only one or two years), we expected the accumulated interseismic displacements to be small compared to the coseismic displacements. Therefore, we constrained secular velocities for all sites to be

zero. Our analysis using FONDA then yields the coseismic displacements given in Table 4A and plotted in Figure 7A. All reported coseismic displacements are relative to the far-field. We obtained similar results for the coseismic displacements (within 0.1 meters) when we constrained secular velocities for all sites to values obtained by combining GPS and triangulation data. Displacement at site P049 was not estimated because only one epoch of measurements was taken at P049 (after the earthquake).

We estimated a total of 4.0 ± 0.6 m of coseismic displacement across the SF (Figure 7A, Table 4A) due to the 1892 earthquake. This estimate is significantly higher than the 2-3 m coseismic displacement reported by *Reid* [1913] based on the same surveys performed by *Müller* [1895]. Some of this discrepancy may be due to the poor quality of available coordinates for S063 and S080. It is also possible that *Reid* [1913] underestimated the coseismic displacements by constraining the positions of stations too close to the fault (P037, P051 and S063).

To assess the magnitude of the 1892 earthquake based on our estimate of surface displacements, we solved for the average coseismic slip on the fault by weighted least-squares inversion of the data, using *Okada's* [1985] formulation of elastic dislocation along a strike-slip fault. We assumed that the 1892 earthquake ruptured the entire main fault zone of the Angkola segment (Figure 1), which we modeled as a vertical (90° dip) fault system consisting of two segments of equal down-dip width, measuring 90 and 56 km along-strike (Figure 7A). The assumed fault lengths were based on the fault segmentation determined by *Sieh and Natawidjaja* [this volume]. We treated our measured surface coseismic displacements as the sum of the effect of coseismic slip on both fault segments. The east and west components of the surface displacements were weighted by their inverse variances in the inversion. We assumed complete rupture along both segments, from a specified fault depth to the surface. We varied this fault depth from 5 to 20 km in 5 km increments. The modeling results are given in Table 5A, and show that the data cannot resolve the depth of coseismic rupture. Figure 7A compares surface displacements predicted by the model for a 5 km rupture depth to those derived from the triangulation data.

We used the estimated coseismic slip and assumed fault plane dimensions to estimate a moment magnitude for the 1892 earthquake using the relationship [*Kanamori*, 1977]:

$$M_w = 2/3\ log_{10}\ M_0\ - 6.0, \qquad (1)$$

where M_0 is the earthquake moment given by [*Brune*, 1968]:

$$M_0 = \bar{u} A\mu\ . \qquad (2)$$

Here $\bar{u}$ is the average coseismic slip on the fault system, A is the area of the fault plane, and μ is the shear modulus (0.4×10^{11} Pa).

For fault depths ranging from 5 to 20 km, we computed an earthquake moment of $M_0 = (3.4 \pm 1.0) \times 10^{20}$ Nm, corresponding to moment magnitudes of $M_w = 7.6$ to 7.7. This estimate is consistent with the comparison of the reported radius of ground-shaking during the 1892 earthquake [*Visser*, 1922] to ground-shaking during nearby earthquakes of known magnitudes, which suggests that the 1892 event had a magnitude of $M_s = 7.7$ or larger [*Natawidjaja*, pers. comm.]. The quality of our data is not sufficient to resolve the down-dip extent of the seismogenic portion of the fault, but is adequate to constrain the moment magnitude of the 1892 earthquake to $M_w \sim 7.6$.

1926 earthquakes

The 1926 earthquakes of Padang Panjang impelled the Dutch colonial government to resurvey sites around the rupture area. Triangulation taken from P001 in 1927 [*Topografische Dienst*, 1927] and from P007 in 1928 [*Topografische Dienst*, 1929], revealed up to 5 arc seconds change in angle measurements. To estimate coseismic displacements due to the 1926 earthquake, we used triangulation measurements from the West Sumatra network, consisting of the measurements taken in 1883-1896, and post-seismic measurements taken in 1927-1930 in the epicentral region. To fix the orientation

and scale of the network, we constrained the positions of the triangulation stations which were surveyed with GPS (P001, P002, P003, P004, P005, P007, P008, P015, P016, P017, P022, P027, and P042), making the assumption that their GPS-updated coordinates are accurate to within half a meter. Since this interval spans a considerable interseismic period, we furthermore assigned secular velocities to the GPS-resurveyed stations, based on the long-term velocities computed from combining the triangulation and GPS measurements (described in the previous subsection of this paper). We estimated interseismic velocities for all other sites, while solving for coseismic displacements at eight sites located near the rupture zone (P007, P008, P009, P015, P016, P017, P019, and P022). We thus assumed that the sites re-measured using GPS have interseismic velocities which are well represented by the combined (GPS + triangulation) solution.

Our best estimates of the 1926 coseismic deformation are given in Table 4B and plotted in Figure 7B. We estimated 1.7 ± 1.0 m of right-lateral displacement across the SF, as shown by the motion of P007 relative to P008 (Figure 7B). Performing this solution using half or twice the interseismic velocities for the sites in question changes the coseismic displacements by up to 1 m in the east component and up to 0.5 m in the north component. The displacement of P007 is best determined because it has the largest number of measurements. Displacements at P008 and P009 are not well constrained because P008 and P009 were only sighted from P007 and other stations before the earthquake, and each have only one angle measurement associated with them during the second epoch. This means that in principle only one component of the displacement at P008 and P009 can be determined. The coseismic displacements reported in Figure 7B represent the best fit to the data, using the stated assumptions for the positions and velocities of the GPS-resurveyed stations.

Recent reinterpretation of *Visser's* [1927] detailed report of the 1926 earthquake, together with independent fieldwork and interviews conducted by *Natawidjaja et al.* [1995] provide us with reasonable limits for the rupture lengths. The August 4, 1926 event consisted of two main shocks of nearly equal magnitude, and appears to have ruptured adjacent fault segments in the vicinity of Lake Singkarak and Lake Maninjau (Figure 7B). *Gutenberg and Richter* [1954] estimated magnitudes of M_s = 6.75 and M_s =

6.5 for the first and second shocks, respectively. *Natawidjaja et al.* [1995] constrained the rupture zone of the first shock to the 58 km fault segment between Alahan Panjang and Lake Singkarak, and the second shock to 64 km between Lake Singkarak and Sipisang, NW and adjacent to the first shock (Figure 7B).

Relying on *Natawidjaja et al.'s* [1995] estimates of fault rupture length, we estimated coseismic slip by weighted least-squares inversion of our estimated 1926 coseismic surface displacements. Again we assumed that rupture occurred on a vertical fault from a specified depth to the surface, and we varied this depth from 5 to 20 km. We performed the inversion using surface displacements for the eight sites listed in Table 4B, weighted by their inverse variances. Results of our inversion are presented in Table 5B and the deformation field predicted by the model for a fault extending down to 15 km is plotted (open arrows) in Figure 7B. From the estimated coseismic slips we computed earthquake moments of $M_0 = (2.4 \pm 1.6) \times 10^{20}$ Nm for the first shock, and $M_0 = (2.6 \pm 1.1) \times 10^{20}$ Nm for the second shock. These moments correspond to M_w = 7.3-7.7 and M_w = 7.4-7.7 for the first (southern) and second (northern) shocks, respectively.

The surface coseismic displacements due to the 1926 earthquake are not well constrained by the data, thus we cannot conclusively place bounds on the moment magnitudes of the events based on the data alone. *Natawidjaja et al.* [1995] concluded from their field surveys that the surface coseismic displacements near the fault were about 2-3 meters, similar to the 1943 event, which also consisted of two main shocks with corrected magnitudes of M_s = 7.1 and M_s = 7.4 [*Pacheco and Sykes*, 1992]. Compared to *Natawidjaja et al.'s* [1995] estimates of coseismic displacements, our estimates of coseismic slips and moment magnitudes from the data inversion are probably too high. In Figure 7B we also plot (gray shaded arrows) the surface coseismic displacements that would result from four meters of slip on both the northern and southern segments (for a fault extending down to 15 km depth). Models with four to five meters of coseismic slip on each fault segment result in WRMS misfits of 2.2 - 2.7 for depths ranging from 5 to 20 km, and correspond to a moment magnitude for each main shock ranging from M_w = 7.1 to M_w = 7.5, respectively. These estimates are more

consistent with *Natawidjaja et al.'s* [1995] field survey results, and are still in reasonable agreement with our data.

In summary, our geodetic results suggest that the 1926 main shocks were significantly larger than previously reported ($M_w \sim 7$ instead of the $M_w \sim 6$ reported by *Gutenberg and Richter* [1954]), and comparable in magnitude to the 1943 events.

1943 earthquakes

The interval between the triangulation and GPS measurements span three $M_w \geq 6$ earthquakes on the SF: the 1943 Padang [*Untung et al.*, 1985], 1977 Pasaman [*Harvard CMT Catalog*], and 1987 Tarutung [*Untung and Kertapati*, 1987] earthquakes. We therefore began our combined estimation by including parameters that allow coseismic displacement at sites located near these three rupture zones. However, the 1977 and 1987 events were not resolvable by our data. Coseismic displacements at P001, P004, and P005 due to the 1943 earthquakes were estimated by constraining the interseismic velocities at those sites to their GPS-determined values. The consistency of this solution is checked by applying the coseismic displacement at those three stations as coseismic corrections in a solution where long-term interseismic velocities for all sites are estimated, as well as small adjustments to the coseismic displacements.

Figure 7C summarizes our estimated coseismic displacements at the three sites due to the 1943 earthquake. The deformation is statistically significant only at P001, where we estimate 0.9 ± 0.3 m displacement (Figure 7C, Table 4C). *Natawidjaja et al.* [1995] reported that the two main shocks (June 8 and 9) of the 1943 event ruptured two adjacent fault segments from south to north, similar to the 1926 event, and estimated rupture lengths of 54 km for the northern event and 46 km for the southern event.

Our estimate of the 1943 coseismic deformation suggests some left-lateral motion at P004, and some fault-normal motion at P001 and P004 (Figure 7C). *Untung et al.* [1985] reported that the coseismic displacements during the 1943 earthquake included significant vertical "scissoring" motion in this area, supporting the notion that faulting in 1943 included a significant dip-slip or thrust component.

The uncertainties of our surface coseismic displacements were too large to allow inversion to estimate fault slip. Therefore, to describe the estimated coseismic deformation field in terms of seismic slip on the fault zone, we implemented *Okada's* [1985] formulation of elastic dislocation in a forward model. We used the rupture fault lengths estimated by *Natawidjaja et al.* [1995], assumed (arbitrarily) that the fault surfaces dip 60° to the NE, and set the fault depth for both segments at 20 km. Varying the amount of strike-slip and thrust-slip, we found that 3 m of left-lateral strike-slip and 0.5 m of thrust-slip on the southern segment, and 2.3 m of right-lateral strike-slip and 1.7 m of thrust-slip on the northern segment yields a reasonable fit to the data. The surface displacements predicted by this 60°-dipping fault model are plotted in Figure 7C. However, none of the fault parameters are uniquely constrained by our data.

Conclusions

By combining triangulation with GPS data, we obtained long-term, near-field velocities along the northern half of the SF. This combined velocity field is consistent with slip rates ranging from ~23 mm/yr to ~24 mm/yr, as inferred from the regional GPS data for the region between 1°S and 2°N, and are within 5 mm/yr of estimates based on earthquake slip vector deflections [*McCaffrey et al.*, this volume]. These rates are fairly consistent with geological estimates by *Sieh and Natawidjaja* [this volume] in the north, but are up to twice as high as their slip rate estimates in the south. The long-term velocity field is also consistent with locking depths on the order of 20 km on the SF. These deep locking depths are consistent with historically high seismicity rates along the SF in the vicinity of the Sumani, Sianok, and Angkola segments and point to continued significant seismic potential in those regions.

Strain rates in the northern back-arc are low, suggesting that the northern back-arc is relatively free of deformation. Strain rates for the Sumani region for the period 1883-1930 are similar to the long term (~100 year) rates, as well as the short-term, GPS-measured rates.

From epochs of triangulation data collected before and after the 1892 and 1926 earthquakes, we estimated coseismic displacements and moment magnitudes. Our results

indicate that these events were larger than previously reported. The 1892 earthquake had a moment magnitude of $M_w \approx 7.6$, and the 1926 main shocks were probably on the order of M_w~7, comparable in size to the 1943 main shocks, instead of M_w~6 as previously reported. We also estimated coseismic displacements for the 1943 earthquake from the combined triangulation and GPS solution, but the fault parameters for this event are poorly constrained by the data.

Acknowledgments. We are indebted to the late Dr. Paul Suharto, deputy and later director of the National Coordination Agency for Surveying and Mapping (BAKOSURTANAL) who passed away in 1999, for his encouragement and support of our work in Indonesia. Site monumentation and data collection for this study could only have been accomplished with the help of many Indonesian, US, and Japanese surveyors. In particular, we would like to mention Agus Soedomo, Chris Bagandi, Heru Derajat, Djawahir, Endang, Nyamadi, Ponimin, Priambodo, Rustandi Poewariardi, Untung Santoso, Bambang Susilo, Widiyanto, and Didi Wikayardi from Indonesia, and Eric Calais, Heather Chamberlain, Dan Johnson, Dalia Lahav, Rob McCaffrey, Brennan O'Neill, Craig Roberts, Jennifer Scott, Bruce Stephens, Briann Wolf, and Peter Zwick from US institutions. The 1989 survey was conducted as a joint effort in conjunction with a research project by Ichiro Murata from Tokyo University. We thank him and the team of Japanese scientists, including Eiji Kawai, Fumiaki Kimata, Satoshi Miura, Shuhei Okubo, and Mikio Satomura, for the excellent collaboration. We are grateful to James Stowell and his staff at the UNAVCO Boulder facility (Bruce Stephens, Mike Jackson) for training and providing field engineers. Joe Bearden at Caltex provided logistical support and GPS receivers for surveys in the Rumbai area, and some welcome R&R at the Caltex facility in Rumbai. From the earliest stages of this project, we are indebted to Ruth Neilan for consolidating the triangulation data, made available to us through BAKOSURTANAL. Klass Villanueva and Joenil Kahar from ITB helped with logistical and other support. We thank Eric Calais, Paul Tregoning and Shimon Wdowinski for their input to the data analysis. Australian tracking data were organized and provided by Ken Alexander, Fritz Brunner, Martin Hendy, John Manning and Paul Tregoning. Miranda Chin and Gerry Mader helped collect regional tracking data during the 1989 Asia-Pacific Experiment (APEX) experiment coordinated with Mike Bevis, and provided CIGNET data. Our IGS colleagues provided global tracking data since 1992. We thank Kerry Sieh and Danny Natawidjaja for useful discussions on many geological aspects of the Sumatran Fault, and to Rob McCaffrey and Shimon Wdowinski for their constructive comments on this paper. John Beavan computed strain rates using ADJCOORD for us. Comments from Jeff Freymueller, Thora Árnadóttir and one

anonymous reviewer helped to improve the manuscript. Figures were drawn with GMT [*Wessel and Smith*, 1991]. Supported at SIO by NSF grants EAR-8817067, EAR-9004376 and NASA grant NAGW-2641, and by the Indonesian government.

References

Bellier, O. and M. Sébrier, Is the slip rate variation on the Great Sumatran Fault accommodated by fore-arc stretching?, *Geophys. Res. Lett., 22*, 1969-1972, 1995.

Bibby, H. M., Unbiased estimate of strain from triangulation data using the method of simultaneous reduction, *Tectonophysics, 82*, 161-174, 1982.

Bock, Y., R. McCaffrey, J. Rais, and I. Murata, Geodetic studies of oblique plate convergence in Sumatra (abstract), *Eos Trans. AGU, 71*, 857, 1990.

Bomford, G., *Geodesy*, 855 pp., Oxford University Press, New York, 1980.

Brune, J. N., Seismic moment, seismicity, and rate of slip along major fault zones, *J. Geophys. Res., 73*, 777-784, 1968.

Collier, P. A., B. Eisfeller, G. W. Hein, H. Landau, On a four-dimensional integrated geodesy, *Bull. Géod., 62*, 71-91, 1988.

Crook, C. N., ADJCOORD: A FORTRAN program for survey adjustment and deformation modeling, N. Z. Geol. Surv. Earth Def. Sec. Rep. 138, 22 pp., Dept. of Sci. Indust. Res., Lower Hutt, New Zealand, 1992.

Davies, R., P. England, B. Parsons, H. Billiris, D. Paradissis, and G. Veis, *J. Geophys. Res., 102*, 24,571-24, 588, 1997.

Defense Mapping Agency, Department of Defense World Geodetic System 1984: its definition and relationships with local geodetic systems, DMA Technical Report, Defense Mapping Agency, Washington, 1987.

Dong, D., The horizontal velocity field in Southern California from a combination of terrestrial and space-geodetic data, Ph.D. Thesis, Mass. Inst. of Technol., Massachusetts, 1993.

Dong, D., T. A. Herring, and R. W. King, Estimating regional deformation from a combination of space and terrestrial geodetic data, *Journal of Geodesy, 72*, 200-214, 1998.

Fang, P. and Y. Bock, Scripps Orbit and Permanent Array Center 1995 Report to IGS in *International GPS Service for Geodynamics 1995 Annual Report*, edited by J. F. Zumberge, M. P. Urban, R. Liu, and R. E. Neilan, p. 103, Jet Propulsion Laboratory, Pasadena, 1996.

Feigl, K., R. W. King, and T. H. Jordan, Geodetic measurement of tectonic deformation in the Santa Maria fold and thrust belt, California, *J. Geophys. Res., 95*, 2679-2699, 1990.

Fitch, T. J., Plate convergence, transcurrent faults and internal deformation adjacent to southeast Asia and the western Pacific, *J. Geophys. Res., 77*, 4432-4460, 1972.

Genrich, J. F., Y. Bock, R. McCaffrey, E. Calais, C. W. Stevens, and C. Subarya, Accretion of the southern Banda arc to the Australian plate margin determined by Global Positioning System measurements, *Tectonics, 15*, 288-295, 1996.

Genrich, J. F., Y. Bock, R. McCaffrey, L. Prawirodirdjo, Fauzi, C. W. Stevens, P. Zwick, S. S. O. Puntodewo, C. Subarya, and J. Rais, Slip distribution at the northern Sumatran Fault System, *this volume*, 2000.

Grant, D. B., Combination of terrestrial and GPS data for earth deformation studies, Ph.D. Thesis, School of Surveying, University of New South Wales, Australia, 1990.

Gutenberg, B. and C. F. Richter, Seismicity of the earth and associated phenomena, *Princeton Univ. Press, Princeton, New Jersey,* 1954.

Hein, G. W., Integrated geodesy state-of-the-art 1986 reference text, in *Lecture Notes in Earth Sciences,* Vol. 7, 505-548, Edited by H. Sunkel, Springer-Verlag, 1986.

Herring, T., Global Kalman filter VLBI and GPS analysis program (GLOBK) version 4.12 and GLORG module 4.04, Mass. Inst. of Technol., Cambridge, Massachusetts, 1997.

International Association of Geodesy, *Geodetic Reference System 1967*, 116 pp., Publication Speciale No. 3, Bureau Central de l'Association Internationale de Géodesie, Paris, 1971.

Kanamori, H., The energy released in great earthquakes, *J. Geophys. Res., 82,* 2981-87, 1977.

King, R. and Y. Bock, Documentation for the GAMIT GPS analysis software release 9.40, Mass. Inst. of Technol. and Scripps Inst. of Oceanog., 1995.

McCaffrey, R., Y. Bock and J. Rais, Crustal deformation and oblique plate convergence In Sumatra (abstract), *Eos Trans. AGU*, 71, 637, 1990.

McCaffrey, R., Slip vectors and stretching of the Sumatra fore arc, *Geology, 19*, 881-884,1991.

McCaffrey, R., P. Zwick, Y. Bock, L. Prawirodirdjo, J. Genrich, S. S. O. Puntodewo and C. Subarya, Strain partitioning in North Sumatra: Geodetic observations and numerical modeling, *this volume*, 2000.

Müller, J. J. A., De verplaasting van eenige triangulatie-pilaren in de residentie Tapanoeli (Sumatra) tengevolge van de aardbeving van 17 Mei 1892, *Natuurk. Tijdscht. v. Ned. Ind., 54*, 299-307, 1895.

Natawidjaja, D. H. and K. Sieh, Slip-rate along the Sumatran transcurrent fault and its tectonic significance, *Proc. Tectonics Evolution Southern Asia*, London, 7-8 Dec., p. 38, 1994.

Natawidjaja, D. H., Y. Kumoro, J. Suprijanto, Gempa bumi tektonik daerah Bukittinggi-Muaralabuh: Hubungan segmentasi sesar aktif dengan gempa bumi tahun 1926 dan 1943, in *Annual convention of Geoteknologi-LIPI*, LIPI, 1995.

Newcomb, K. R. and W. R. McCann, Seismic history and seismotectonics of the Sunda Arc, *J. Geophys. Res., 92*, 421-439, 1987.

Okada, Y., Surface deformation due to shear and tensile faults in a half-space, *Bull. Seismol. Soc. Amer., 75*, 1135-1154, 1985.

Pacheco, J. F. and L. R. Sykes, Seismic moment catalog of large shallow earthquakes, 1900 to 1989, *Bull. Seismol. Soc. Amer., 82*, 1306-1349, 1992.

Prawirodirdjo, L., Y. Bock, R. McCaffrey, J. Genrich, E. Calais, C. Stevens, S. S. O. Puntodewo, C. Subarya, J. Rais, P. Zwick and Fauzi, Geodetic observations of interseismic strain segmentation at the Sumatra subduction zone, *Geophys. Res. Lett., 24*, 2601-2604, 1997.

Prawirodirdjo, L., A geodetic study of Sumatra and the Indonesian region: Kinematics and crustal deformation from GPS and triangulation, Ph.D. Thesis, University of California, San Diego, 2000.

Puntodewo, S. S. O., R. McCaffrey, E. Calais, Y. Bock, J. Rais, C. Subarya, R. Poewariardi, C. Stevens, J. Genrich, Fauzi, P. Zwick and S. Wdowinski, GPS

measurements of crustal deformation within the Pacific-Australia Plate Boundary Zone in Irian Jaya, Indonesia, *Tectonophysics*, *237*, 141-153, 1994.

Reid, H. F., Sudden earth-movements in Sumatra in 1892, *Bull. Seismol. Soc. Amer.*, *3*, 72-79, 1913.

Savage, J. C. and R. O. Burford, Geodetic determination of relative plate motion in central California, *J. Geophys. Res.*, *78*, 832-845, 1973.

Segall, P. and M. V. Matthews, Displacement calculations from geodetic data and the testing of geophysical deformation models, *J. Geophys. Res.*, *93*, 14,954-14,966, 1988.

Sieh, K., J. Rais and Y. Bock, Neotectonic and paleoseismic studies in west and north Sumatra (abstract), *EOS Trans. AGU, 72*, 460, 1991.

Sieh, K. and D. Natawidjaja, Neotectonics of the Sumatran Fault, *this volume*, 1999.

Sillard, P., Z. Altamimi and C. Boucher, The ITRF96 realization and its associated velocity field, *Geophys. Res. Lett.*, *17*, 3223-3226, 1998.

Snay, R. and A. R. Drew, Combining GPS and classical geodetic surveys for crustal deformation in the Imperial Valley, California, in *High Precision Navigation—Integration of Navigational and Geodetic Methods, Springer-Verlag,* New York, 225-236, 1989.

Stevens, C., R. McCaffrey, Y. Bock, J. Genrich, Endang, C. Subarya, S. S. O. Puntodewo, Fauzi and C. Vigny, Rapid rotations about a vertical axis in a collisional setting revealed by the Palu fault, Sulawesi, Indonesia, *Geophys. Res. Lett.*, *26*, 2677-2680, 1999.

Topografische Dienst, Jaarverslag van den Topografischen Dienst in Nederlandsch Indie over 1927, 23ste Jaargang, Topografische Inrichting, Batavia, 1927.

Topografische Dienst, Jaarverslag van den Topografischen Dienst In Nederlandsch Indie over 1928, 24ste Jaargang, Topografische Inrichting, Batavia, 1929.

de Triangulatiebrigade van den Topografischen Dienst, Driehoeksnet van Sumatra's Westkust - De Coördinaten der driehoekspunten, Topografische Inrichting, Batavia, 1916.

Untung, M., N. Buyung, E. Kertapati, Undang, and C. R. Allen, Rupture along the Great Sumatran Fault, Indonesia, during the earthquakes of 1926 and 1943, *Bull. Seismol. Soc. Amer., 75*, 313-317, 1985.

Untung, M. and E. K. Kertapati, Aspek seismologi gempa bumi Tarutung, 27 April 1987, Kabupaten Tapanuli, Sumatra Utara (unpublished paper), Simposium Gempa Tarutung 27 April 1987, Universitas Kristen Indonesia, 1987.

Visser, S. W., Inland and submarine epicentra of Sumatra and Java earthquakes, *Koninklijk magnetisch en meteorologisch observatorium te Batavia, 9*, 1-14, 1922.

Visser, S. W., De aardbevingen in de Padangsche Bovenlanden, *Natuurk. Tijds. v. Ned. Indie*, 36-71, 1927.

War Research Institute, Triangulation in Sumatra and its outliers, Office of the Geodetic Branch, Survey of India, 1944.

Wessel, P., and W. H .F. Smith, Free software helps map and display data, *Eos Trans. AGU, 72*, 441, 1991.

Yu, E. and P. Segall, Slip on the 1868 Hayward earthquake from the analysis of historical triangulation data, *J. Geophys. Res., 101*, 16101-18118, 1996.

Zhang, J., Y. Bock, H. Johnson, P. Fang, J. Genrich, S. Williams, S. Wdowinski, and J. Behr, Southern California Permanent GPS Geodetic Array: Error analysis of daily position estimates and site velocities, *J. Geophys. Res., 102*, 18,035-18,055, 1997.

Figure Captions

Figure 1. Map of the West and North Sumatra region with bathymetry (500 m contour intervals), tectonic features, and inset showing geographic location. The Sumatran fault trace is based on data collected by *Sieh and Natawidjaja* [this volume], and fault segments discussed in the text are labeled in bold italics with names and dates of earthquake occurrences. Arrows in the Indian Ocean and at the trench show the direction and rates of convergence of the Australia plate relative to Southeast Asia. Open arrows show slip orientation on the Sumatran Fault, with slip rates from GPS measurements reported by *Genrich et al.* [this volume].

Figure 2. Historical triangulation and GPS networks in Sumatra. Sites connected by solid lines indicate triangulation sites used in this study. Black crosses indicate triangulation sites with more than one epoch of observation. Circles indicate GPS survey sites. Shaded areas are rupture zones of the 1892, 1926, and 1943 earthquakes. Sites discussed in the text are labeled with site names. Some of the triangulation sites which were resurveyed with GPS were renamed in the process (see Table 2). These sites are labeled with both triangulation and GPS site codes, separated by a slash. Sites belonging to the "North Sumatra" and "West Sumatra " networks are listed in Table 1. Subnetworks are labeled in bold.

Figure 3. Photographs showing different types of Sumatra triangulation monuments surveyed with GPS. (A) and (B) show primary pillars (P106 and P109) that have remained intact since the 1880s, including their brass survey markers. Shape and height of the pillars often required metal extension rods (shown in (A)) for the survey tripods in order to center the antenna accurately above the survey mark. (C) A well-preserved secondary pillar (S200). (D) At other sites like S58, the pillar was still erect but damaged, with no trace of the bronze marker. We placed stainless steel pins at the center of the top surface to serve as the GPS survey mark. (E) Some monuments, such as P005, had suffered heavy damage over the years. In such cases a new concrete monument was reconstructed over the still recognizable foundation of the original pillar. Horizontal

location of the original survey marker could often be identified and "recovered" to within tens of centimeters.

Figure 4. Histogram of residuals from adjustment of 374 horizontal angles in the 1883-1896 survey, calculated with P037 and P042 fixed (see text). Solid line represents a normal distribution with zero mean and standard deviation of 0.4 arc seconds.

Figure 5. Interseismic velocity field (solid arrows) derived from a combination of triangulation and GPS observations. Open arrows are 1989-1993 GPS-derived velocities from *Genrich et al.* [this volume], shown for comparison. Ellipses indicate 95% confidence levels.

Figure 6. Fault-parallel components of velocities derived from triangulation and GPS data (circles) with associated formal one standard deviation as a function of orthogonal distance across segments of the Sumatran Fault. Solid lines are fault-parallel velocity profiles from *Genrich et al.* [this volume], reflecting the best-fitting (in a least squares sense) slip rates and locking depths inferred from GPS data. The velocity field is divided into sections corresponding to fault segments as reported by *Sieh and Natawidjaja* [this volume] (see Figure 1).

Figure 7A. Sites comprising *Müller's* [1895] survey network (triangles) overlie a radar image of the region surrounding the Sumatran Fault equatorial bifurcation. Radar image courtesy of BAKOSURTANAL, Indonesia. 1892 Tapanuli earthquake displacements computed from triangulation taken before and after the earthquake (gray shaded arrows), with 95% confidence ellipses. Open arrows show results of our elastic dislocation modeling. Heavy black lines indicate the trace of the model fault plane. Model parameters are explained in the text and in Table 5. Numerical values of the coseismic displacements are given in Table 4.

Figure 7B. 1926 Padang Panjang earthquake displacements, computed from triangulation measurements taken before and after the event (solid arrows). Open and

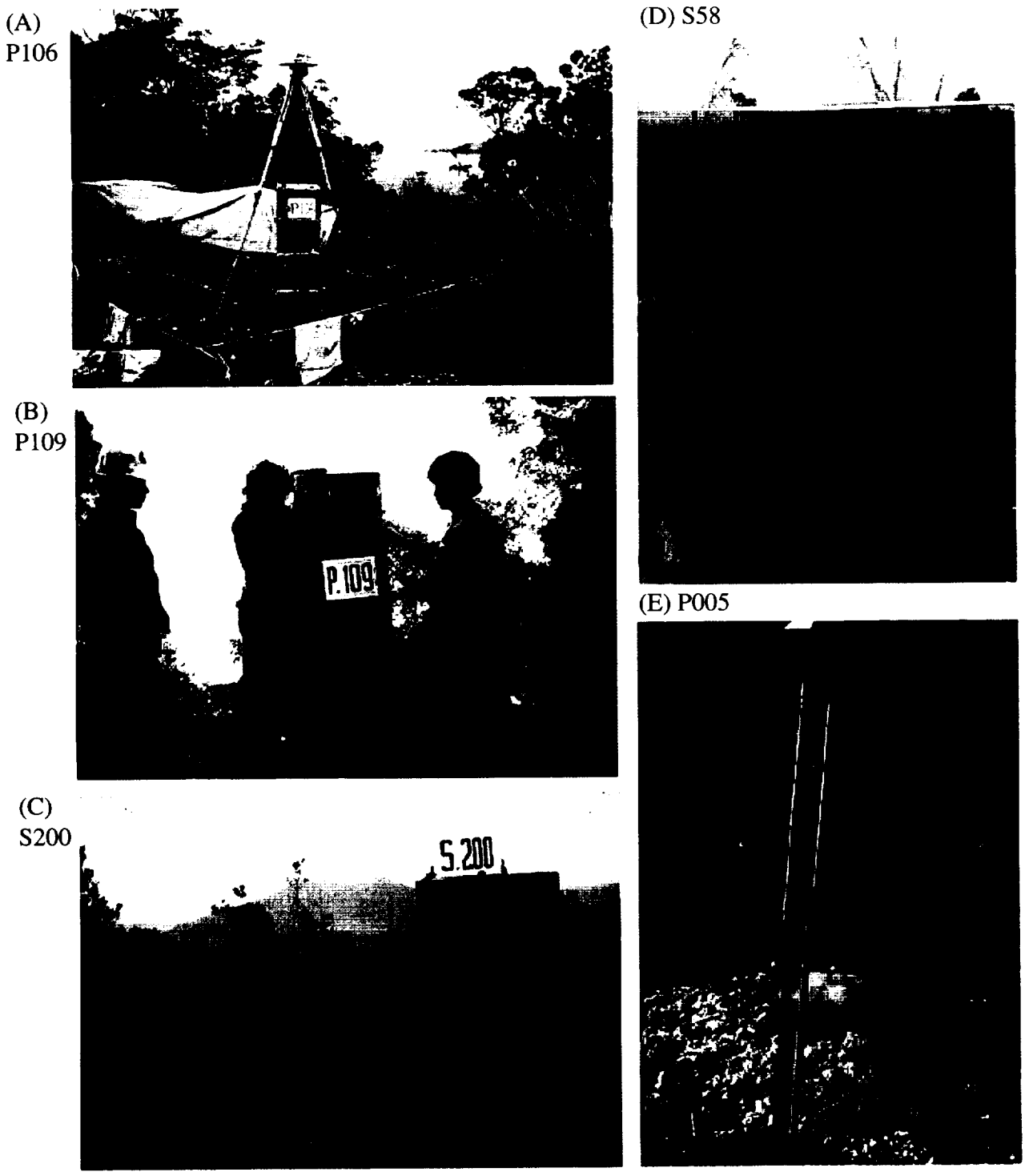

Figure 3

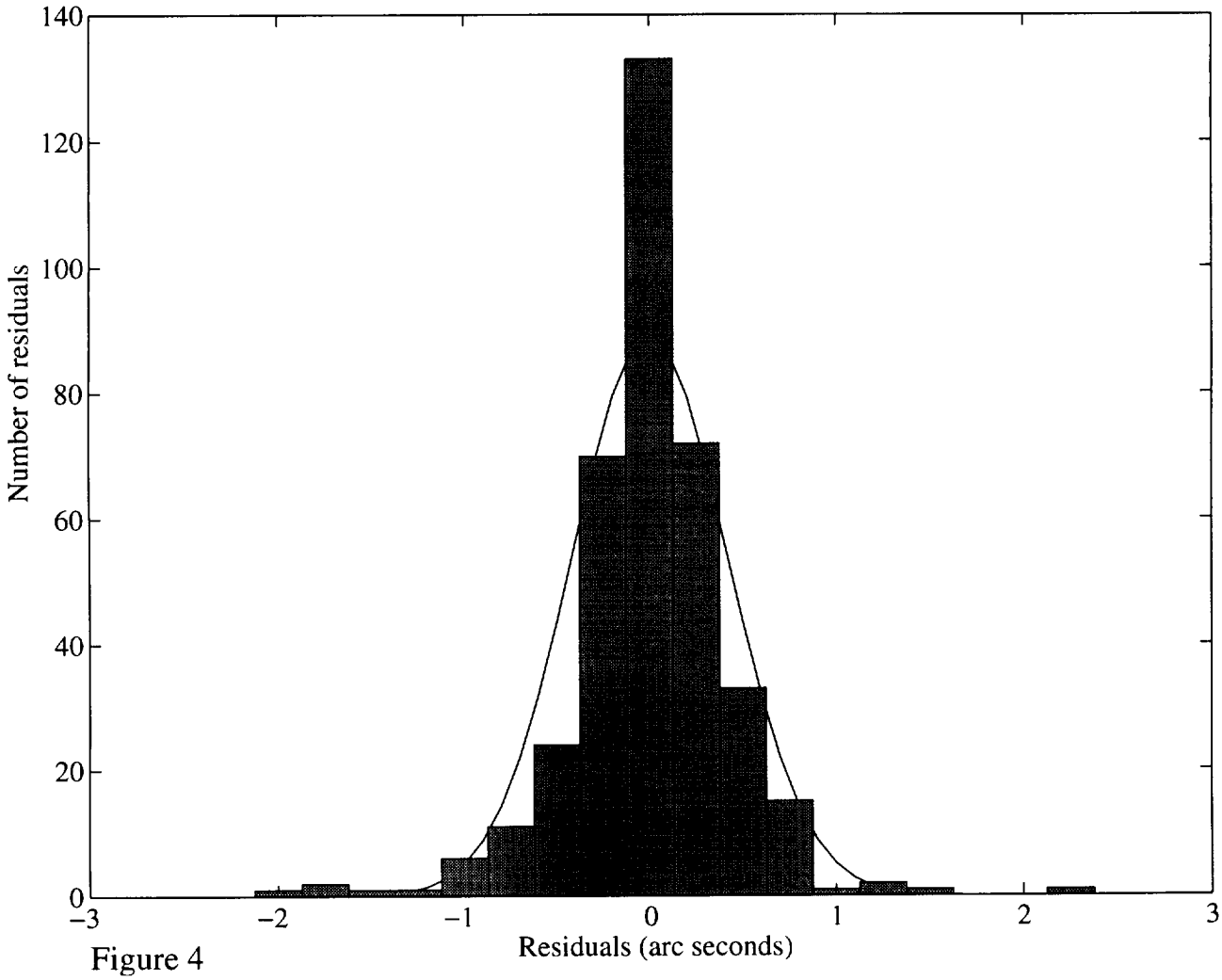
140
120
100
80
60
40
20
0
Number of residuals
−3
−2
−1
0
1
2
3
Residuals (arc seconds)

Figure 4

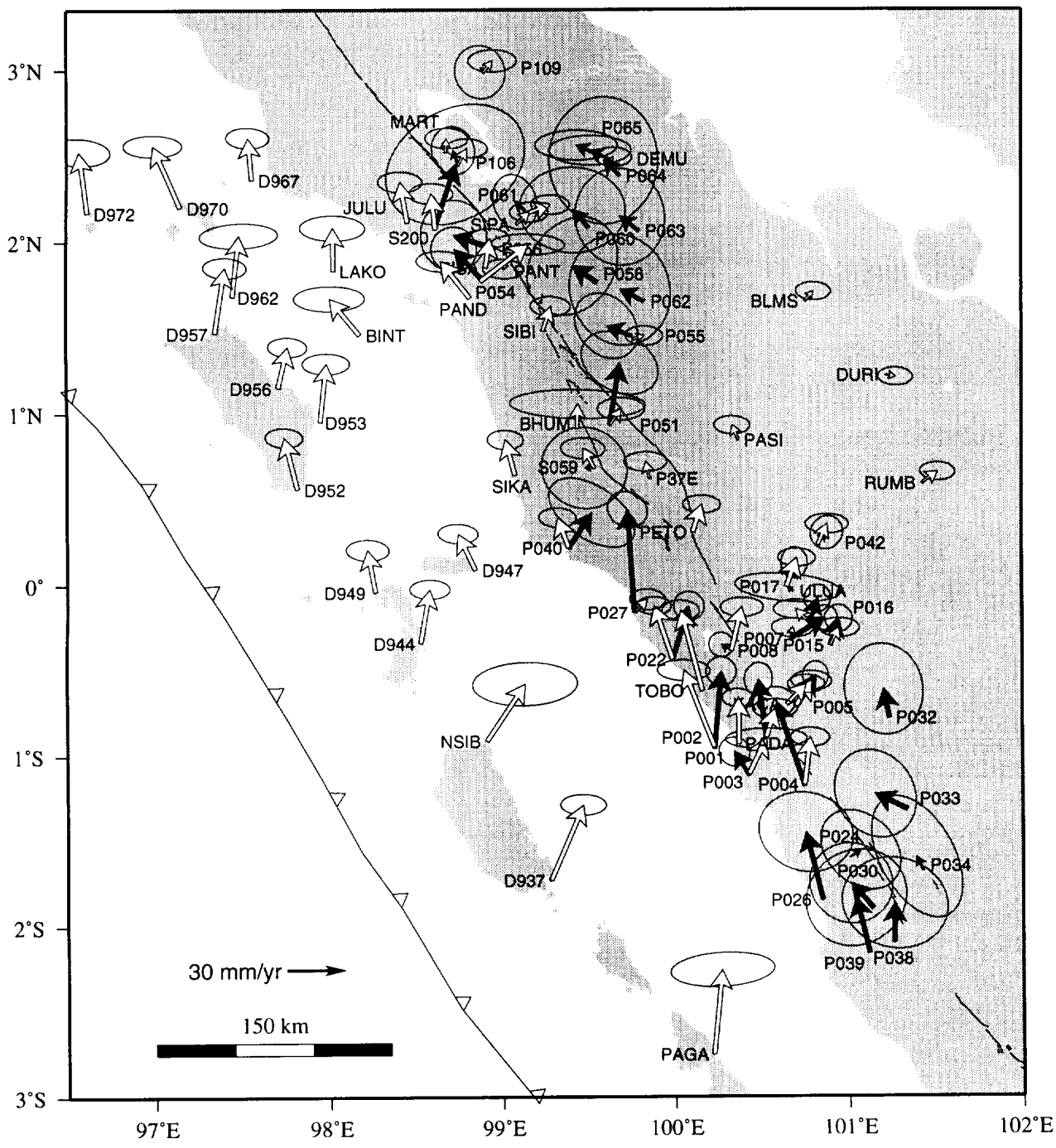
3°N
2°N
1°N
0°
1°S
2°S
3°S
97°E
98°E
99°E
100°E
101°E
102°E
P109
MART
P106
P065
DEMU
P064
D967
D972
D970
P061
JULU
SIPA
S200
P063
P060
LAKO
PANT
P058
D962
P054
PAND
P062
BLMS
D957
BINT
SIBI
P055
DURI
D956
D953
BHUM
P051
PASI
D952
S059
SIKA
P37E
RUMB
P040
PETO
P042
D947
D949
P017
P016
P027
P007
P015
D944
P008
P022
TOBO
P005
P032
NSIB
P002
P001
P003
P004
P033
P024
P030
P034
D937
P026
P039
P038
30 mm/yr
150 km
PAGA

Figure 5

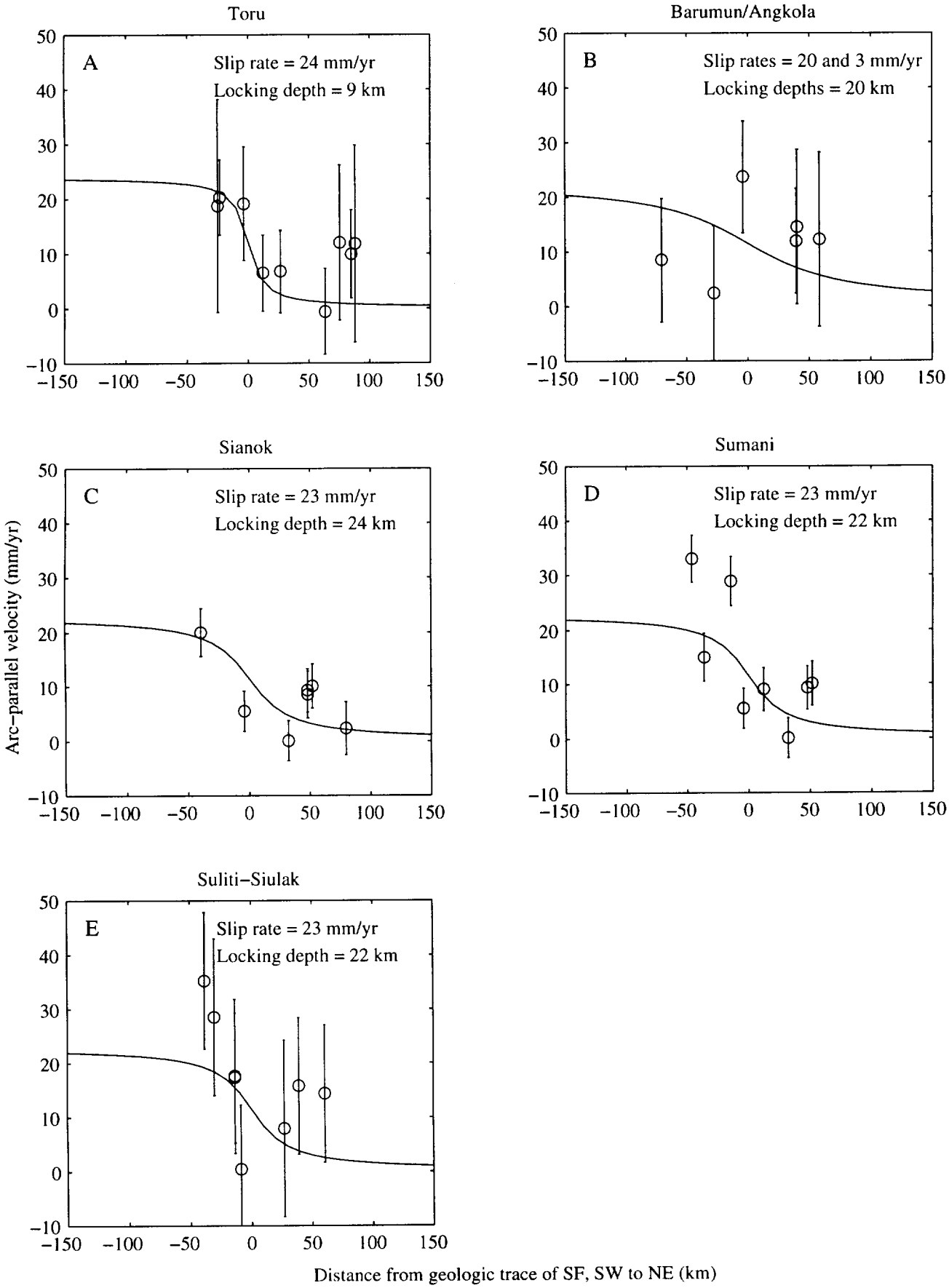
Toru
A
Slip rate = 24 mm/yr
Locking depth = 9 km
Barumun/Angkola
B
Slip rates = 20 and 3 mm/yr
Locking depths = 20 km
Sianok
C
Slip rate = 23 mm/yr
Locking depth = 24 km
Sumani
D
Slip rate = 23 mm/yr
Locking depth = 22 km
Suliti–Siulak
E
Slip rate = 23 mm/yr
Locking depth = 22 km
Arc–parallel velocity (mm/yr)
Distance from geologic trace of SF, SW to NE (km)

Figure 6

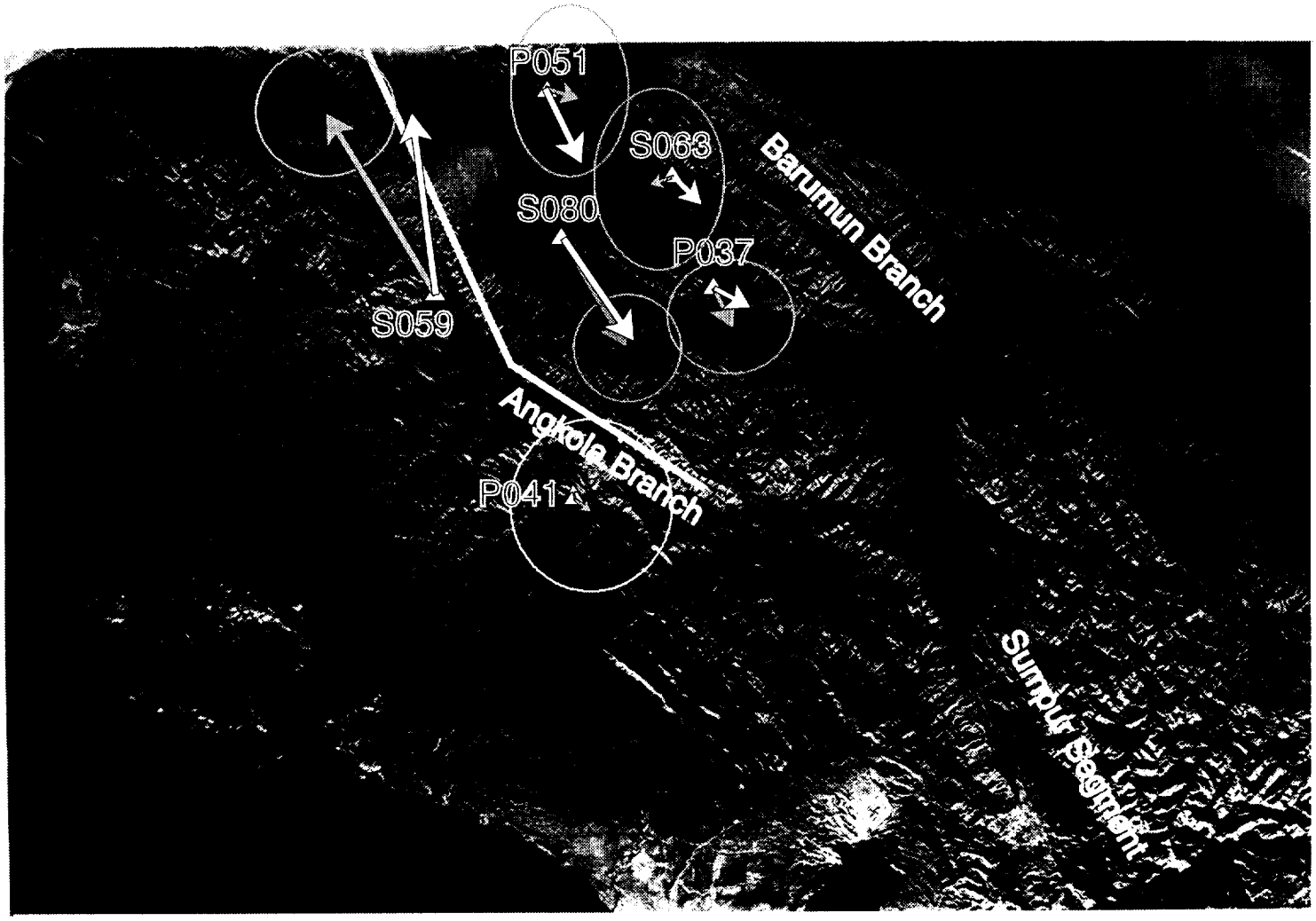
P051
S063
S080
P037
S059
Barumun Branch
Angkola Branch
P041
Sumpur Segment
150 km
2 meters

Figure 7a

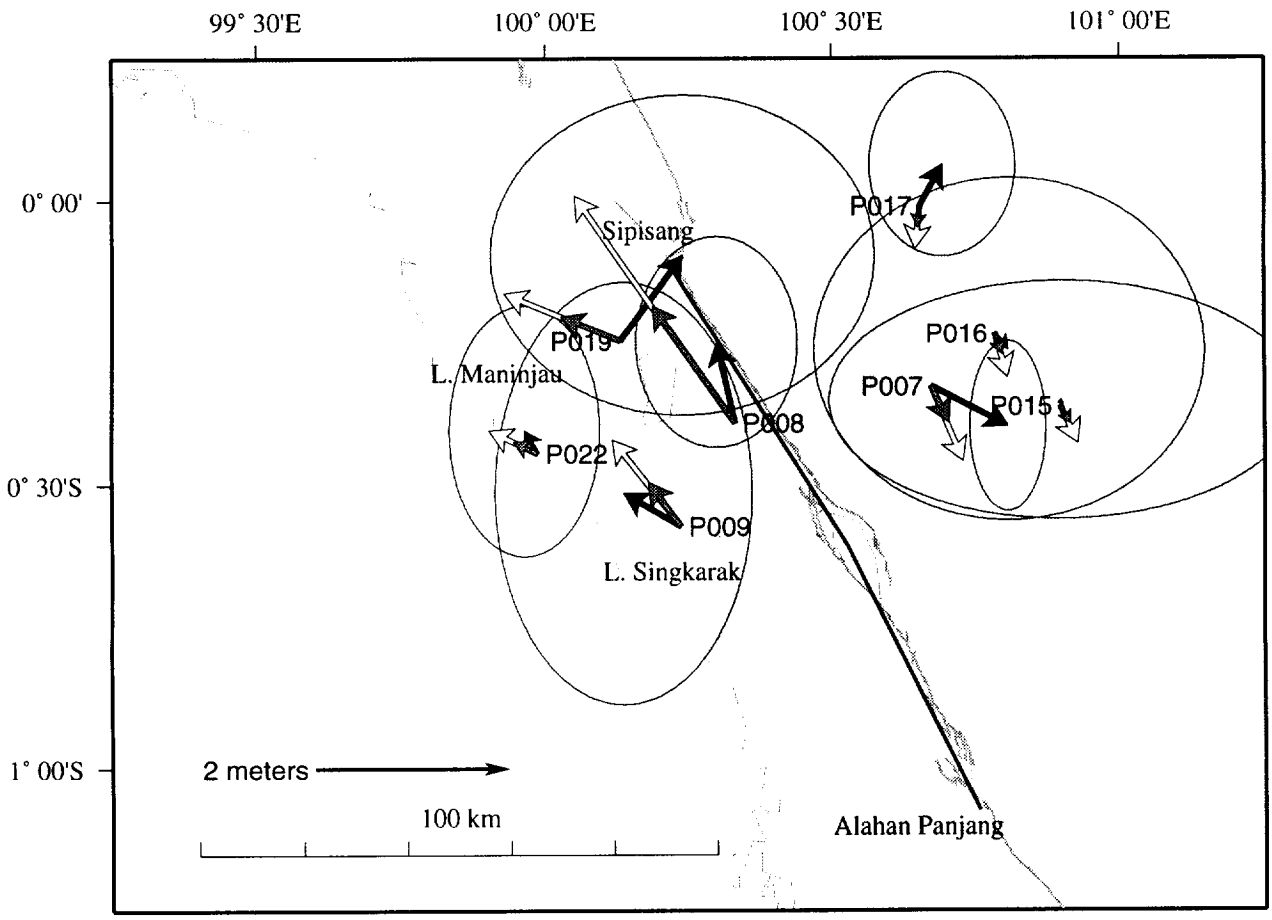
99° 30'E
100° 00'E
100° 30'E
101° 00'E
0° 00'
0° 30'S
1° 00'S
Sipisang
P017
P019
L. Maninjau
P016
P007
P015
P008
P022
P009
L. Singkarak
2 meters
100 km
Alahan Panjang

Figure 7B

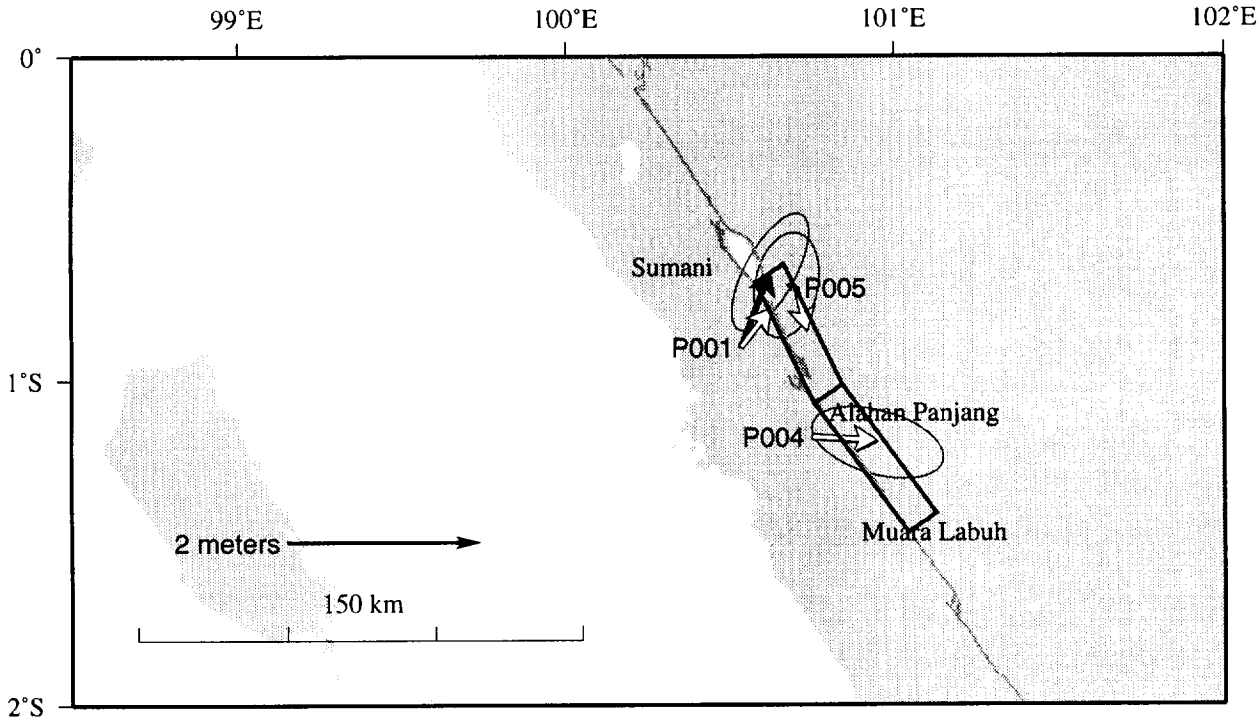
99°E
100°E
101°E
102°E
0°
1°S
2°S
Sumani
P005
P001
Alahan Panjang
P004
Muara Labuh
2 meters
150 km

Figure 7C

Table 1A. West Sumatra Triangulation Network: station coordinates (WGS84) and calendar years of survey.

Site Code	Lat. (N)	Lon. (E)	Triangulation surveys in	GPS surveys in
P001	-0.8992	100.5337	1883,1884,1885,1927,1930	1991,1993
P002	-0.9560	100.2308	1883,1884,1885,1927,1930	1991,1993
P003	-1.1166	100.4293	1883,1884,1885,1927,1930	1990,1993
P004	-1.1769	100.7504	1885,1886,1887,1927,1930	1991,1993
P005	-0.7159	100.7037	1883,1885,1886,1927,1930	1991,1993
P006	-0.7256	100.4582	1883,1885,1927,1928	-
P007	-0.3245	100.6731	1885,1886,1887,1928	1991,1993
P008	-0.3899	100.3311	1885,1886,1928	1991,1993
P009	-0.5724	100.2368	1884,1885,1927	-
P010	-1.3677	100.6090	1885,1887	-
P011	-1.2777	100.8021	1885,1887	-
P012	-1.2465	101.0131	1886,1887,1888,	-
P013	-0.9879	101.0827	1885,1886,1917,1930	-
P014	-0.5861	100.9833	1886,1930	-
P015	-0.3612	100.8985	1885,1886,1887,1928	1991,1993
P016	-0.2323	100.7850	1885,1886,1887,1928	1991,1993
P017	-0.0075	100.6538	1885,1887,1928	1990,1993 (as DING)
P018	0.0753	100.3893	1885,1886,1887,1888,1928	-
P019	-0.2452	100.1309	1885,1886,1930	-
P020	-0.4112	100.1794	1885,1886,1930	-
P021	-0.5959	100.0748	1885,1930	-
P022	-0.4444	99.9867	1885,1886,1930	1989,1990,1991,1993 (as TANJ)
P023	-0.2662	99.8846	1885,1886,1930	-
P024	-1.5980	101.0098	1887,1888,1889,1917,1918	-
P025	-1.6079	100.6414	1885,1887,1888	-
P026	-1.8474	100.8503	1887,1888,1889,1890,1918	-
P027	-0.1584	99.7655	1885,1886,1890	1989,1990,1991,1993 (as AJUN)
P028	0.0787	99.9839	1885,1886,1888,1890	-
P030	-1.9006	101.1387	1887,1888,1889,1890,1917, 1918	-
P031	-1.0189	101.2732	1886,1887,1888	-
P032	-0.7751	101.2399	1886,1917	-
P033	-1.3242	101.3418	1886,1887,1888,1917	-
P034	-1.6778	101.4280	1887,1888, 1917,1918	-
P035	0.3093	100.1904	1887,1888,1891	-
P036	0.7364	100.2429	1887,1888,1891	-
*P037	0.7018	99.8199	1888,1890,1891, 1892	-
P038	-2.1010	101.2631	1889,1890,1904	-
P039	-2.1604	101.1209	1888,1889,1890,1904	-
P040	0.2226	99.3879	1885,1890,1891	1989,1990,1991,1993 (as AIRB)

*P041	0.4770	99.6513	1885,1888,1890,1891,1892, 1893	1993 (data are bad)
P042	0.2372	100.8324	1886,1887	1989,1990,1991,1993 (as PAUH)
P043	0.4097	100.6978	1887,1888,1891	-
P047	-2.5413	101.4393	1890, 1904	-
*P049	0.7562	99.2753	1890,1891,1892,1893,1894	-
P050	1.4782	99.2096	1893,1894,1895	-
*P051	0.9439	99.6261	1890,1891,1892,1893,1894	1991,1993
P052	0.3439	99.1288	1890,1891,1893	-
P053	0.8388	98.9818	1891,1893,1894	-
P054	1.7859	98.8779	1894,1895	1990,1993 (as GADI)
P055	1.4489	99.7553	1894,1895	1989,1990,1991,1993 (as BINA)
P056	1.9599	98.9682	1894,1895,1908,1913	-
P057	1.2710	98.8258	1893,1894	-
P058	1.7572	99.5604	1894,1895,1930	-
P059	1.8756	99.1724	1894,1895,	-
P060	2.0830	99.5083	1894,1895,1930	-
P061	2.1770	99.1364	1895,1908,1912	1989,1990,1993
P062	1.6480	99.8344	1894,1895,1930	-
P063	2.0605	99.7981	1894,1895,1930	-
P104	-2.2277	101.4272	1890,1917,1918	-
*S059	0.6861	99.5393	1890,1891,1892,1893	1990,1993 (as MERA)
*S063	0.8605	99.7678	1891,1892,1893	-
*S080	0.7686	99.6401	1891,1892,1893	-
S174	-1.8980	101.7749	1887,1917,1918	-

*Sites comprising Müller's survey network that spanned the 1892 Tapanuli earthquake

Table 1B. North Sumatra Triangulation Network: station coordinates (WGS84) and calendar years of survey.

Site Code	Lat. (N)	Lon. (E)	Triangulation surveys in	GPS surveys in
P064	2.3782	99.6871	1895,1913,1930	-
P065	2.5083	99.5534	1913	-
P066	2.4524	99.3570	1912,1913	-
P106	2.4622	98.7463	1908,1912	1989,1990,1993 (as DOLO)
P107	2.5982	99.0654	1908,1909	-
P108	2.6854	98.6090	1908,1909	-
P109	3.0130	98.9036	1908,1909	1990, 1993 (as DSIM)
P110	2.9259	98.5354	1908,1909	-
P111	3.2474	98.5006	1909,1910,1914,1915	-
P112	3.1376	98.1267	1909,1910	-
P121	2.1958	98.5976	1908,1913	-
S103	2.1726	99.3616	1913	-
S104	2.0763	98.8257	1908,1913	-
S200	2.0922	98.6153	1908,1913	1990,1991,1993 (as SIGL)

Table 2. North and West Sumatra historical triangulation sites re-surveyed with GPS in 1989-1993

Trig. site code	GPS site code	Relation of GPS survey mark to original trig. marker	Uncertainty of GPS survey mark w.r.t. trig. mark[b](cm)	Est. offset between trig. & eccentric site[c]	
				azimuth (°)	distance (km)
[a]P001	P001	Monument reconstructed	10	-	-
[a]P002	P002	Monument reconstructed	10	-	-
[a]P003	P003	Monument reconstructed	10	-	-
[a]P004	P004	Monument reconstructed	10	-	-
[a]P005	P005	New monument reconstructed over center of foundation's remains	100	-	-
[a]P007	P007	Monument reconstructed	10	-	-
[a]P008	P008	Original monument, no bronze marker	10	-	-
[a]P015	P015	Monument reconstructed	10	-	-
P016	P016	Monument reconstructed	20	-	-
[a]P017	DING	Monument reconstructed	10	-	-
	ULUA	Eccentric point to P017	-	297	5
P022	TANJ	Monument reconstructed	10	-	-
[a]P027	AJUN	Monument reconstructed on foundation remains	10	-	-
P037	P37E	Eccentric point to P037	-	327	8.75
P035	PETO	Eccentric point to P035	-	124	10
[a]P040	AIRB	Monument reconstructed	10	-	-
[a]P042	PAUH	Original monument	5	-	-
P050	SIBI	Eccentric point to P050	-	225	4
P051	P051	Monument reconstructed	20	-	-
[a]P054	GADI	Original monument found tilted	10	-	-
	PISA	Eccentric point to P054	-	125	13.75
[a]P055	BINA	Monument reconstructed	50	-	-
P059	PANT	Eccentric point to P059	-	116	14
[a]P061	P061	Monument reconstructed over original foundation	10	-	-

P065	DEMU	Original monument destroyed - eccentric point constructed to P065	-	291	8
[a]P106	DOLO	Original monument	5	-	-
	MART	Eccentric point to P106	-	141	12.25
[a]P109	DSIM	Original monument	5	-	-
[a]S059	MERA	Original monument	5	-	-
[a]S200	SIGL	Original monument	5	-	-

[a]Sites which were used to estimate transformation parameters between the triangulation and GPS coordinates.

[b]For collocated sites; not applicable to eccentric sites.

[c]Only applicable to eccentric sites.

Table 3. Horizontal Interseismic Strain Rates

Region name	$\dot{\varepsilon}_{11}$ (10^{-6}/yr)	$\dot{\varepsilon}_{22}$ (10^{-6}/yr)	θ (°)	$\dot{\gamma}_1$ (10^{-6}/yr)	$\dot{\gamma}_2$ (10^{-6}/yr)	N	Source of estimate
Sumani	-0.10 ± 0.04	0.09 ± 0.07	24.8 ± 10.9	0.13 ± 0.09	-0.15 ± 0.08	16	1989-1993 GPS *McCaffrey et al.* [2000]
Sumani	-0.09 ± 0.03	0.14 ± 0.03	32.4 ± 2.9	0.09 ± 0.02	-0.3 ± 0.02	9	1883-1885 to 1989-1993 triangulation and GPS
Sumani	-	-	31.0 ± 12.9	0.08 ± 0.08	-0.15 ± 0.07	21	1883-1885 to 1927-1930 triangulation
Back-arc	-0.01 ± 0.03	0.02 ± 0.08	168.1 ± 12.6	0.03 ± 0.07	0.014 ± 0.06	8	1989-1993 GPS *McCaffrey et al.* [2000]
Northern back-arc	-	-	not well determined	0.03 ± 0.12	0.06 ± 0.09	6	1893-1895 to 1930 triangulation

Strain rates are expressed in terms of the axes of maximum compression ($\dot{\varepsilon}_{11}$) and extension ($\dot{\varepsilon}_{22}$) and the engineering shear strain rates $\dot{\gamma}_1$ and $\dot{\gamma}_2$. θ is the azimuth of maximum contraction. N is the number of sites used in the strain estimation. Quoted uncertainties are formal standard errors.

Table 4A. 1892 Tapanuli earthquake coseismic horizontal displacements. Quoted uncertainties represent one standard deviation.

Site	East component (m)	North component (m)
P037	0.3 ± 0.3	-0.6 ± 0.3
P041	0.2 ± 0.4	-0.2 ± 0.5
P051	0.5 ± 0.3	-0.1 ± 0.4
S059	-1.5 ± 0.4	2.4 ± 0.3
S063	-0.3 ± 0.4	-0.1 ± 0.5
S080	0.8 ± 0.3	-1.4 ± 0.3

Table 4B. 1926 Padang Panjang earthquake coseismic horizontal displacements. Quoted uncertainties represent one standard deviation.

Site	East component (m)	North component (m)
P007	0.8 ± 0.2	-0.4 ± 0.4
P008	-0.2 ± 0.3	0.8 ± 0.4
P009	-0.6 ± 0.5	0.3 ± 0.9
P015	0.0 ± 1.0	0.1 ± 0.5
P016	0.1 ± 0.8	-0.2 ± 0.7
P017	0.2 ± 0.3	0.4 ± 0.4
P019	0.6 ± 0.8	0.9 ± 0.7
P022	-0.1 ± 0.3	0.2 ± 0.5

Table 4C. 1943 Padang earthquake coseismic horizontal displacements. Quoted uncertainties represent one standard deviation.

Site	East component (m)	North component (m)
P001	0.3 ± 0.2	0.8 ± 0.3
P004	0.7 ± 0.3	-0.1 ± 0.2
P005	-0.1 ± 0.1	0.0 ± 0.2

Table 5A. Coseismic slip on fault surfaces estimated by weighted least-squares inversion of surface displacements for 1892 earthquake. Uncertainties are formal one standard deviation.

Downdip fault width (km)	$\bar{u}_1$ [average coseismic slip on southern segment] (m)	$\bar{u}_2$ [average coseismic slip on northern segment] (m)	weighted RMS (m)
5	2 ± 8	12 ± 4	1.2
10	1 ± 6	8 ± 4	1.4
15	1 ± 5	6 ± 3	1.5
20	1 ± 5	6 ± 3	1.6

Positive values for $\bar{u}_1$ and $\bar{u}_2$ indicate right-lateral slip. Both fault segments are assumed to be vertical (dip = 90°) and of equal downdip width. Model parameters are discussed further in the text.

Table 5B. Coseismic slip on fault surfaces estimated by weighted least-squares inversion of surface displacements for 1926 events. Uncertainties are formal one standard deviation.

Downdip fault width (km)	$\bar{u}_1$ [average coseismic slip on southern segment] (m)	$\bar{u}_2$ [average coseismic slip on northern segment] (m)	weighted RMS (m)
5	7 ± 9	12 ± 7	2.4
10	9 ± 9	9 ± 6	1.9
15	9 ± 8	8 ± 4	1.7
20	8 ± 8	7 ± 4	1.5

Positive values for $\bar{u}_1$ and $\bar{u}_2$ indicate right-lateral slip. Both fault segments are assumed to be vertical (dip = 90°) and of equal downdip width. Model parameters are discussed further in the text.

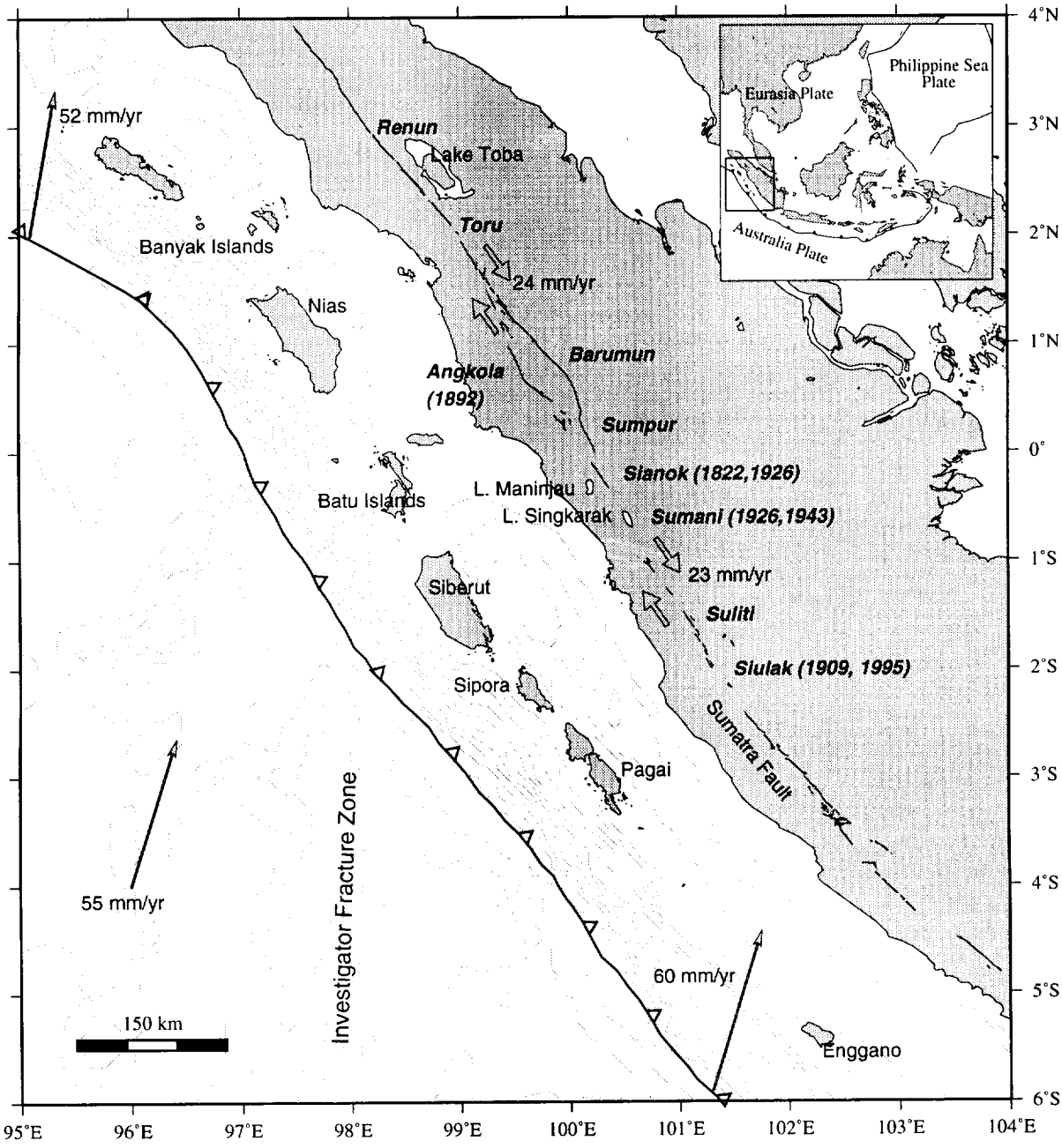
52 mm/yr
Renun
Lake Toba
Toru
24 mm/yr
Banyak Islands
Nias
Angkola
(1892)
Barumun
Sumpur
Sianok (1822,1926)
L. Maninjau
L. Singkarak
Sumani (1926,1943)
Batu Islands
23 mm/yr
Siberut
Suliti
Siulak (1909, 1995)
Sipora
Sumatra Fault
Pagai
55 mm/yr
Investigator Fracture Zone
60 mm/yr
150 km
Enggano
Eurasia Plate
Philippine Sea Plate
Australia Plate
4°N
3°N
2°N
1°N
0°
1°S
2°S
3°S
4°S
5°S
6°S
95°E
96°E
97°E
98°E
99°E
100°E
101°E
102°E
103°E
104°E

Figure 1

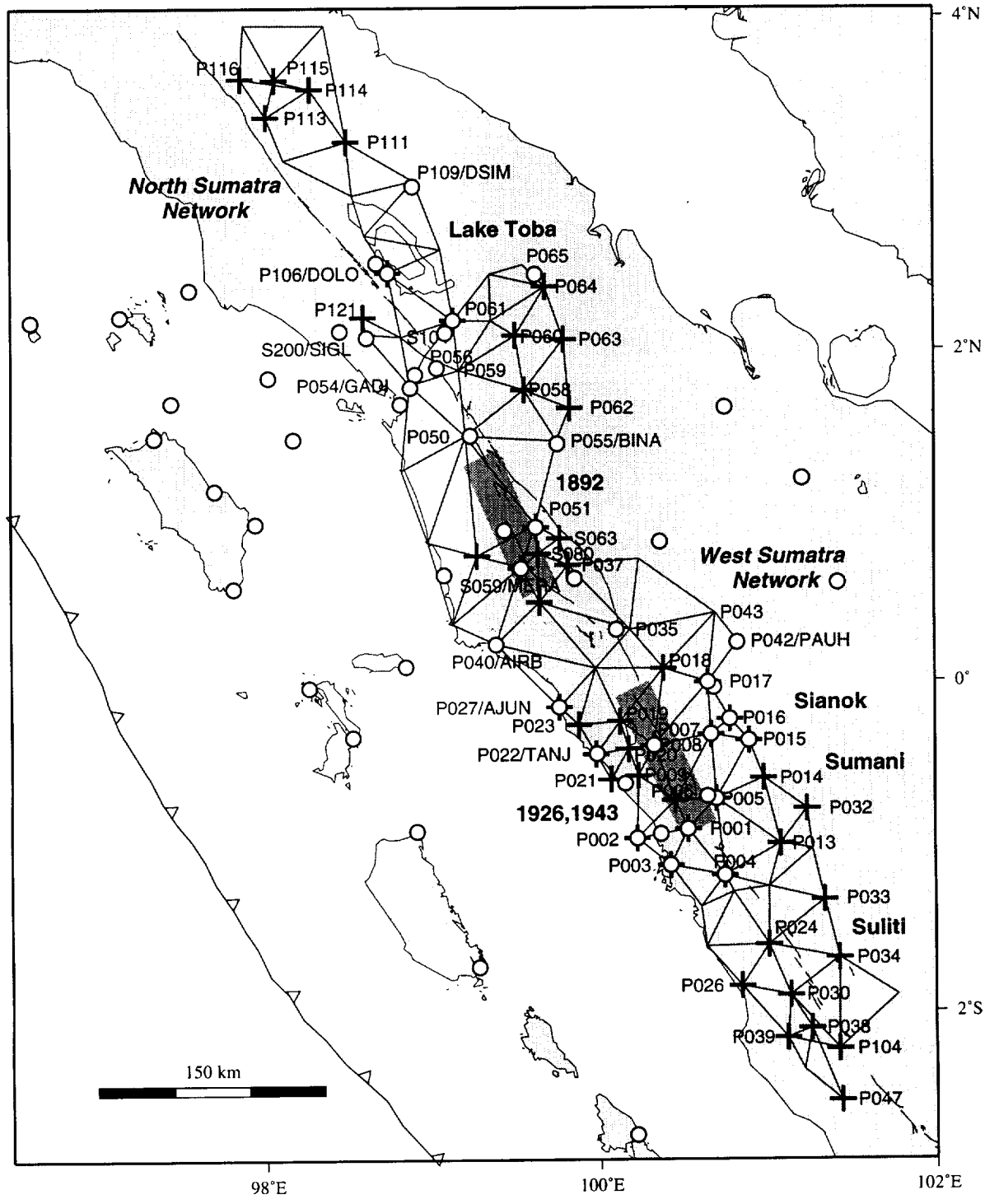
P116
P115
P114
P113
P111
P109/DSIM
North Sumatra Network
Lake Toba
P065
P106/DOLO
P064
P121
P061
S10
P060
P063
S200/SIGL
P056
P059
P054/GADU
P058
P062
P050
P055/BINA
1892
P051
S063
S060
P037
West Sumatra Network
S059/MEPA
P043
P035
P042/PAUH
P040/AIRB
P018
P017
Sianok
P027/AJUN
P023
P016
P007
P008
P015
P022/TANJ
Sumani
P021
P014
P005
P032
1926,1943
P001
P002
P013
P003
P004
P033
P024
Suliti
P034
P026
P030
P038
P039
P104
P047
150 km
4°N
2°N
0°
2°S
98°E
100°E
102°E

Figure 2

gray shaded arrows show results of our elastic dislocation modeling (see text for explanation). The first main shock in 1926 ruptured between Alahan Panjang and L. Singkarak, and the second between L. Singkarak and Sipisang.

Figure 7C. Coseismic displacements for the 1943 Padang earthquake computed from triangulation and GPS measurements (solid arrows). Open arrows show results of our elastic dislocation modeling. The first main shock ruptured between Muara Labuh and Alahan Panjang, and the second between Alahan Panjang and Sumani.